



Supplementary Material for

Electronic dura mater for long-term multimodal neural interfaces

Ivan R. Mineev, Pavel Musienko, Arthur Hirsch, Quentin Barraud, Nikolaus Wenger, Eduardo Martin Moraud, Jérôme Gandar, Marco Capogrosso, Tomislav Milekovic, Léonie Asboth, Rafael Fajardo Torres, Nicolas Vachicouras, Qihan Liu, Natalia Pavlova, Simone Duis, Alexandre Larmagnac, Janos Vörös, Silvestro Micera, Zhigang Suo, Grégoire Courtine,* Stéphanie P. Lacour*

*Corresponding author. E-mail: gregoire.courtine@epfl.ch (G.C.); stephanie.lacour@epfl.ch (S.P.L.)

Published 9 January 2015, *Science* **347**, 159 (2015)

DOI: 10.1126/science.1260318

This PDF file includes:

Materials and Methods
Supplementary Text
Table S1
Figs. S1 to S18
Full Reference List

Other Supplementary Material for this manuscript includes the following:

(available at www.sciencemag.org/content/347/6218/159/suppl/DC1)

Movies S1 to S3

Materials and Methods

Soft e-dura materials and fabrication process

We designed and fabricated brain and spinal e-dura implants using soft neurotechnology. The spinal implant hosts seven electrodes, distributed along the length of the implant in a 3-1-3 configuration array, and a microfluidic delivery system (single channel). The brain implant consists of electrodes, patterned in a 3x3 matrix. A generic fabrication process is presented **fig. S2**. The fabrication steps of the three components integrated in e-dura implants are detailed below.

Interconnects (fig. S2-1)

- i) First a 100 μ m thick substrate of polydimethylsiloxane (PDMS, Sylgard 184, Dow Corning, mixed at 10:1, w:w, pre-polymer:cross-linker) was spin-coated on a 3" silicon carrier wafer pre-coated with polystyrene sulfonic acid (water soluble release layer). The PDMS substrate was then cured overnight in a convection oven (80°C).
- ii) Then a customized Kapton[®] shadow mask patterned with the negative of the electrode layout was laminated on the PDMS substrate. Thermal evaporation of 5/35nm of chromium/gold (Cr/Au) metal films through the shadow mask deposited the interconnect tracks (Auto 360, Edwards).

Electrical passivation layer (fig. S2-2)

- i) The interconnect passivation layer was prepared in parallel. A 5" wafer sized, 5mm thick slab of PDMS was produced and its surface was functionalized with a 1H,1H,2H,2H-perfluorooctyltriethoxysilane (Sigma-Aldrich) release monolayer under weak vacuum. Two thin PDMS layers of 20 μ m thickness were sequentially spin-coated on the thick PDMS slab, individually cured then treated with the debonding monolayer. In cross-section, the structure was a triple stack consisting of a thick PDMS slab and two thin PDMS layers. The release coatings allowed for each of the 20 μ m thick layers to be peeled off independently at a later stage.
- ii) Using a hollow glass capillary of a pre-defined tip diameter, both 20 μ m thick PDMS layers were simultaneously punctured at locations corresponding to the sites of the electrodes.

Encapsulation (fig. S2-3)

- i) Both PDMS triple stack and interconnect wafers were exposed to brief air plasma activating the silicone surfaces. The triple stack was flipped upside down to align the punctured holes with the underlying electrodes.
- ii) The two pieces were brought together to form a covalent bond. The thick PDMS slab was peeled off, leaving behind the two 20 μ m thick PDMS layers on top of the interconnects.

Soft platinum-silicone composite preparation and patterning (fig. S2-4)

- i) e-dura electrode sites were coated with a customized platinum-silicone composite. The conductive composite was a blend of platinum nano-micro particles and PDMS (Sylgard 184, Dow Corning). The PDMS pre-polymer, mixed with its cross-linker, was diluted in heptane in a 1:2 w:w ratio to create a low viscosity liquid. In a small container, 100mg of platinum microparticles (Pt powder, particle size 0.5-1.2 μ m, Sigma-Aldrich) was added to 5mg of PDMS (15 μ L of heptane diluted PDMS). This mixture was thoroughly stirred and put aside for evaporation of the heptane fraction. The addition of 5mg doses of PDMS was repeated until the mixture (after heptane evaporation) became a paste. Paste formation occurs when the PDMS content is 15-20% by weight. Immediately before dispensing onto the electrode sites, the paste may be thinned with a drop of pure heptane.
- ii) To form the active electrode coating, a bolus of conductive composite paste was “printed” i.e. spread and pressed into the holes of the upper encapsulation layer.
- iii) The upper encapsulation layer was then peeled off, leaving bumps of conductive composite precisely at the active electrode sites. The bottom 20 μ m thick PDMS layer remained permanently bonded to the electrode-interconnect e-dura substrate, thereby providing electrical encapsulation. The array was placed in a convection oven at 60°C overnight to ensure full polymerization of the conductive paste.

Microfluidic and connector integration (fig. S2-5)

- i) To form the microfluidic delivery system, an additional 80 μ m thick PDMS layer was bonded to the metallized e-dura substrate. This layer covered approximately a third of the length of the implant and contained a central microfluidic channel (100x50 μ m² in cross section), terminating 2 mm caudally from the 3 caudal electrodes (Movie S1). The connector side of the microchannel was interfaced with a polyethylene capillary (0.008” i.d., 0.014” o.d., Strategic Applications Inc.) and sealed with a bolus of fast-cure silicone (KWIK-SIL, World Precision Instruments).
- ii) A custom-made soft-to-wires electrical connector was assembled for all the e-dura implants. De-insulated ends of ‘Cooner’ wires (multistranded steel insulated wire, 300 μ m o.d., Cooner wire Inc.) were carefully positioned above the terminal pads of the gold film interconnects. The electrical contact was enhanced by ‘soldering’ the wires to the contact pads with a conductive polymer paste (H27D, component A, EPO-TEK) deposited below and around each electrical wire. To stabilize the connector, the ‘solder’ connection area was flooded with a silicone adhesive to form a package (One component silicone sealant 734, Dow Corning) (**Fig. 1D**).

Release (fig. S2-6)

- i) The contour of the finished implant was cut out from the wafer using a razor blade. The implant was released from the carrier wafer upon a brief immersion in water.

Description of the implants prepared for the biocompatibility study

For the purpose of the biocompatibility study, we designed and fabricated soft e-dura and stiff implants. Four copies of each type were fabricated and implanted chronically in the subdural space of the lumbosacral spinal cord in healthy rats.

Soft implants

The e-dura were functional silicone implants, including both the microfluidic channel and seven electrodes, and were designed to fit the intrathecal space of the spinal cord. The implants were prepared following the process presented above.

Stiff implants

Stiff implants were cut out from 25 μ m thick polyimide foil (KaptonTM-100HN, DuPont). The intraspinal dwelling portion of these devices was 3.2mm wide and 3cm long. The contour of the implant was cut out using a laser micromachining tool (LAB 3550, Inno6 Inc.) and had rounded edges to minimize tissue trauma during insertion. At its caudal end, the implant integrated the same trans-spinal electrical connector as the one used in the soft implants. However, neither electrodes nor interconnects were patterned on the polyimide foil. The dummy connector was 8mm long, 11mm wide and 2mm thick and coupled seven insulated wires (multistranded steel insulated wire, 300 μ m o.d., Cooner wire Inc.) that run sub-cutaneous away from the spinal orthosis to a head mounted socket (12 pin male micro-circular connector, Omnetics corp.).

Sham-operated rats

Sham-operated rats received an implant without intraspinal portion. The implant consisted of the same connector as that used in the other two types of implants, which was secured with the spinal orthosis, and then attached to seven wires running subcutaneously, and terminating in a head-mounted Omnetics connector.

Mechanical spinal cord model (fig. S9A)

We assembled a spinal cord model to simulate the mechanical interaction between spinal tissue and soft versus stiff implants after their positioning on the spinal tissue and during dynamic movement of the spinal cord. Artificial dura mater and spinal tissues were fabricated from PDMS and gelatin hydrogel, respectively (23, 31). One end of a polystyrene rod (20cm long, 3.2mm diameter) was attached to the drive shaft of a mixer. The mixer was positioned so that the rod was horizontal and rotating about its long axis, approximately a centimeter above the surface of a hotplate. Several grams of freshly prepared PDMS pre-polymer (Sylgard 184, Dow Corning) were dispensed along the length of the rotating rod. By adjusting the rotation speed, the distance between rod and hotplate, and the hotplate temperature, the thickness of the PDMS film that coated the polystyrene rod was controlled. Following thorough curing of the silicone coating, the polystyrene core was dissolved by immersion in acetone overnight. Thorough rinsing and de-swelling of the silicone in water left a PDMS tube with wall thickness ranging 80-

120 μ m. One end of the tube was pinched and sealed with a bolus of fast-cure silicone (KWIK-SIL, World Precision Instruments), the other end was trimmed to a total tube length of 8.5 cm. Artificial spinal tissue was fabricated by pouring warm ($\approx 40^{\circ}\text{C}$) gelatin solution (10% gelatin by weight in water, gelatin from bovine skin, Sigma-Aldrich) into a silicone mold containing a cylindrical cavity, 3.2mm in diameter and 10cm long. The mold was then placed in a fridge for 1h to allow for the gel to set. The gelatin ‘spinal tissue’ was recovered from the mold and placed in a desiccator under mild vacuum for several hours. Partial loss of water content caused shrinkage and stiffening of the gelatin ‘spinal tissue’. This allowed for its insertion inside the surrogate dura mater tube together with a stiff or soft implant. The assembled model was then immersed in water overnight to re-hydrate the hydrogel ‘spinal tissue’ and secure the implant in the artificial intrathecal space. The open end of the model was then sealed with quick setting silicone and the model was ready for mechanical tests.

Verification of the compression modulus of the hydrogel was conducted through an indentation test. A large slab (6cm thickness, 12cm diameter) of gelatin hydrogel was prepared and indented with a spherical indenter (6mm diameter) mounted on a mechanical testing platform (Model 42, MTS Criterion). By fitting a Hertz contact model to experimental force versus displacement data we obtained a compressive elastic modulus of 9.2 ± 0.6 kPa (n=5 test runs) for the 10% gelatin hydrogel. Indentation of rat spinal cords yields closely comparable values (32).

In vitro electrochemical characterization of e-dura electrodes

In vitro Electrochemical Impedance Spectroscopy of e-dura electrodes under stretch (Fig. 3A, 3E, fig. S13)

We developed an experimental set-up combining electrochemical impedance spectroscopy with cyclic mechanical loading. The e-dura implant under test was mounted in a customized uni-axial stretcher and immersed in saline solution to conduct electrochemical characterization of the electrodes following different stretching protocols.

Electrochemical Impedance Spectroscopy measurements were conducted in phosphate buffered saline (PBS, pH 7.4, Gibco) at room temperature using a three-electrode setup and a potentiostat equipped with a frequency response analyzer (Reference 600, Gamry Instruments). A 5cm long Pt wire served as counter electrode and a Standard Calomel Electrode (SCE) as reference. Impedance spectra were taken at the open circuit potential. The excitation voltage amplitude was 7mV. Impedance spectra of individual electrodes were measured at tensile strains of 0%, 20% and 45%.

Stretching in PBS of the e-dura implants was conducted in a LabView-controlled, custom-built uniaxial tensile stretcher programmed to actuate two clamps moving in opposite directions along a horizontal rail. Each clamp held a stiff plastic rod pointing downwards from the plane of motion. The lower halves of the rods were submerged in a vessel holding electrolyte. The device under test was attached to the submerged part of the rods with silicone glue (KWIK-SIL, World Precision Instruments), so that the motion of the clams was transferred to the device under

test (**Movie S1**). The stretcher was programmed to hold the implant under test at a specific strain or to execute a pre-set number of stretch-relaxation cycles (for example 0%-20%-0% at a stretch rate of 40%/s).

Cyclic Voltammetry (CV) of electrodes under stretch (Fig. 3B)

CV responses were recorded in 0.15M H₂SO₄ (pH 0.9) under N₂ purge. A potential scan rate of 50mV/s was used within the potential range of -0.28V to +1.15V (vs. SCE). Due to the difference in pH, this potential range corresponds to -0.6V to +0.8V (vs. SCE) in PBS. For each tested electrode, 20 priming cycles (1,000mV/s) were applied to allow the electrode to reach a steady state.

Charge injection capacity (CIC) of e-dura electrodes (fig. S12, Fig. 3C)

CIC is a measure of the maximum charge per phase per unit area an electrode coating can deliver through reversible surface reactions. For CIC determination, electrodes with the platinum-silicone composite coating were immersed in PBS and cathodic-first, biphasic current pulses (200μs per phase) were passed between the electrode and a large platinum counter electrode. A pulse stimulator (Model 2100, A-M Systems) delivered the current pulses, and the electrode polarization (vs. SCE) was recorded on an oscilloscope (DPO 2024 Digital Phosphor Oscilloscope, Tektronix). The amplitude of the current pulses was gradually increased until the electrode under test was polarized just outside the water window (the instantaneous polarization of the electrodes due to Ohmic resistances in the circuit was subtracted from voltage traces).

For experiments where the CIC was determined after cyclic pulse delivery, the repeating pulses were charge balanced, biphasic (200μs per phase) with amplitude of 100μA.

In vivo Electrochemical Impedance Spectroscopy of e-dura electrodes (fig. 3E)

The impedance of e-dura electrodes implanted over lumbosacral segments were recorded using a bipolar electrode configuration (working and counter electrode only). The counter electrode was a ‘Cooner’ wire whose de-insulated tip was implanted in the osseous body of vertebra L1. As with in vitro measurements, impedance spectra were obtained with a potentiostat equipped with a frequency response analyzer (Reference 600, Gamry Instruments) using the same settings. Weekly electrochemical impedance spectroscopy measurements of all electrodes were made in fully awake rats held by an experienced handler.

Scanning Electron Microscopy of e-dura electrodes (fig. S14)

Scanning electron microscopy (Zeiss Merlin FE-scanning electron microscope) was used to visualize e-dura electrodes under tensile strain. Prior to imaging, a 5nm thick layer of platinum was sputtered on the implant under investigation. To image the electrode active sites under tensile strain in situ, the e-dura implant was mounted and stretched in a custom-made miniature stretcher that can be inserted in the microscope chamber.

Mechanical characterization of the platinum-silicone composite (fig. S3)

A block of platinum-silicone composite was cut to produce a high aspect-ratio pillar of 3mm height and 480 μ m x 110 μ m rectangular base. The sample was glued to a glass slide so that the pillar's long axis was vertical (sticking out of the plane of the glass slide). A miniature force probe (FT-S10000 Lateral Microforce Sensing Probe, FemtoTools) applied a force at the tip of and normal to the pillar. Using beam bending theory, the geometry of the beam, and its force-displacement characteristics, we computed a value for the composite's Young's modulus of 10 MPa.

Tensile mechanical properties of rat spinal cord (Fig. 1B)

A section of rat dura mater was explanted from a 2-month old Lewis rat and cut to a strip with dimensions of 3.4mm x 1mm. Immediately post explantation, each end of the strip was secured to a glass cover slip using a fast acting cyanoacrylate adhesive. The cover slips were inserted into the clamps of a tensile testing platform (Model 42, MTS Criterion). Extension at strain rate of 0.5%/s was continuously applied until the dura mater sample failed. The thickness of the dura mater sample was determined from optical micrographs. During the process of mounting and stretching, the dura mater sample was kept hydrated with saline dispensed from a micropipette. The stress(strain) response plotted **Fig. 1B** for spinal tissues was adapted from  1).

Animal groups and surgical procedures

All surgical procedures were performed in accordance with Swiss federal legislation and under the guidelines established at EPFL. Local Swiss Veterinary Offices approved all the procedures. Experiments were performed on Lewis rats (LEW/ORLj) with initial weight of 180-200g.

Animal groups

- In the biocompatibility study, rats received either a sham (n=4), stiff (n=4) or soft (n=4) implant. Prior to surgery rats were handled and trained daily in the locomotor tasks for three weeks. These tasks included walking overground along a straight runway, and crossing a horizontal ladder with irregularly spaced rungs. Prior to the training, rats underwent a mild food deprivation and were rewarded with yoghurt at the end of each trial. The body weight was monitored closely; in case of weight loss the food deprivation was adjusted. The animals were terminated 6 weeks post-implantation.
- In the study with electrochemical spinal cord stimulation, rats (n=3) were first implanted with an e-dura over lumbosacral segments, and with bipolar electrodes into ankle muscles to record electromyographic (EMG) activity. After 10 days of recovery from surgery, they received a spinal cord injury.

- Recording of electrospinograms were obtained in a separate group of rats that were implanted with an e-dura over lumbosacral segments, and with bipolar electrodes into ankle muscles of both legs. Recordings were obtained after 6 weeks of implantation.
- Recording of electrocorticograms were obtained in a group of rats (n = 3) that were implanted with an e-dura over the leg area of the motor cortex, and with bipolar electrodes into ankle muscles of both legs. These rats followed the same behavioral training as rats in the biocompatibility group.
- Recording of electrocorticograms following optical stimulation were obtained in Thy1-ChR2-YFP transgenic mice (Jackson Laboratories, B6.Cg-Tg-(Thy1-COP4/EYFP)18Gfng/J) under acute, anesthetized conditions.

Implantation of e-dura into the spinal subdural space (fig. S5A-B)

The e-dura were implanted under Isoflurane/Dorbene anesthesia. Under sterile conditions, a dorsal midline skin incision was made and the muscles covering the dorsal vertebral column were removed. A partial laminectomy was performed at vertebrae levels L3-L4 and T12-T13 to create entry and exit points for the implant. To access the intrathecal space, a 3mm long mediolateral incision was performed in the dura mater at both laminectomy sites. A loop of surgical suture (Ethilon 4.0) was inserted through the rostral (T12-T13) dura mater incision and pushed horizontally along the subdural space until the loop emerged through the caudal (L3-L4) dura mater incision. The extremity of the implant was then folded around the suture loop. The loop was then retracted gently to position the implant over the spinal cord. A small portion of the implant protruded beyond the rostral dura mater incision and could be manipulated with fine forceps to adjust the mediolateral and rostrocaudal positioning of the implant. Electrophysiological testing was performed intra-operatively to fine-tune positioning of electrodes with respect to lumbar and sacral segment L50). The protruded extremity of the implant became encapsulated within connective tissues, which secured positioning of the implant in the chronic stages.

The soft-to-wires (and microfluidic) connector was secured to the bone using a newly developed vertebral orthosis. The connector was first positioned above the vertebral bone. Four micro-screws (Precision Stainless Steel 303 Machine Screw, Binding Head, Slotted Drive, ANSI B18.6.3, #000-120, 0.125) were inserted into the bone of rostral and caudal vertebrae. Surgical suture (Ethilon 4.0) was used to form a cage around the micro-screws and connector. The walls of the cage were plastered using freshly mixed dental cement (ProBase Cold, Ivoclar Vivadent) extruded through a syringe. After solidification of the dental cement, the electrical wires and microfluidic tube were routed sub-cutaneously to the head of the rat, where the Omnetics electrical connector and the microfluidic access port were secured to the skull using dental cement. The same method was used to create the vertebral orthosis for stiff and sham implants in the biocompatibility study.

Implantation of e-dura into the cortical subdural space (fig. S5C-D)

The e-dura were implanted under Isoflurane/Dorbene anesthesia. Under sterile conditions, 2 trepanations were performed on the left half of the skull to create two windows rostral and caudal to the leg area of the motor cortex. The first window was located cranially with respect to the coronal suture, while the second window was located cranially with respect to the interparietal suture. Both windows were located close to sagittal suture in order to position the center of the e-dura electrodes 1 mm lateral and 1mm caudal relative to the bregma. The surgical insertion technique developed for passing e-dura into the spinal subdural space was also used to implant e-dura into the cortical subdural space. Excess PDMS material was cut in the cranial window, and the edge of the implants sutured to the dura mater using a Ethilon 8.0 suture. The exposed parts of the brain and external part of the e-dura were covered with surgical silicone (KWIK-SIL). A total of 4 screws were implanted into the skull around the e-dura connector before covering the entire device, the connector, and the percutaneous amphenol connector with dental cement.

Implantation of electrodes to record muscle activity

All the procedures have been reported previously (30). Briefly, bipolar intramuscular electrodes (AS632; Cooner Wire) were implanted into the tibialis anterior and medial gastrocnemius muscles, bilaterally. Recording electrodes were fabricated by removing a small part (1mm notch) of insulation from each wire. A common ground wire (1cm of Teflon removed at the distal end) was inserted subcutaneously over the right shoulder. All electrode wires were connected to a percutaneous amphenol connector (Omnetics Connector Corporation) cemented to the skull of the rat. The proper location of EMG electrodes was verified post-mortem.

Spinal cord injury

Under Isoflurane/Dorbene anesthesia, a dorsal midline skin incision was made from vertebral level T5 to L2 and the underlying muscles were removed. A partial laminectomy was performed from around T8 to expose the spinal cord. The exposed spinal cord was then impacted with a metal probe with a force of 250 kDyn (IH-0400 Impactor, Precision Systems and Instrumentation). The accuracy of the impact was verified intra-operatively, and all the lesions of the animals used in this study were reconstructed post-mortem.

Rehabilitation procedures after spinal cord injury

Rats with severe contusion spinal cord injury were trained daily for 30min, starting 7 days post-injury. The neurorehabilitation program was conducted on a treadmill using a robotic bodyweight support system (Robomedica) that was adjusted to provide optimal assistance during bipedal stepping (30). To enable locomotion of the paralyzed legs, a serotonergic replacement therapy combining quipazine (0.03 ml) and 8-OHDPAT (0.02 ml) was administered through the microfluidic channel of chronically implanted e-dura, and tonic electrical stimulation was delivered through the electrodes located overlying the midline of lumbar (L2) and sacral (S1) segments (40Hz, 0.2ms pulse duration, 50-200 μ A (30)).

Histology and Morphology of explanted spinal cord

Fixation and explantation

At the end of the experimental procedures, rats were perfused with Ringer's solution containing 100 000 IU/L heparin and 0.25% NaNO₂ followed by 4% phosphate buffered paraformaldehyde, pH 7.4 containing 5% sucrose. The spinal cords were dissected, post-fixed overnight, and transferred to 30% phosphate buffered sucrose for cryoprotection. After 4 days, the tissue was embedded and the entire lumbosacral tract sectioned in a cryostat at a 40µm thickness.

3D reconstruction of the spinal cord (Fig. 2B, fig. S7)

To assess spinal cord morphology, a Nissl staining was performed on 25 evenly spaced lumbosacral cross-sections separated by 0.8 mm, for each rat. The slides were assembled into the Neurolucida image analysis software (MBF Bioscience, USA) to reconstruct lumbosacral segments in 3D. Spinal cord compression was quantified using a circularity index defined as 4π area/perimeter². Circularity index was measured for all the slices, and averaged for each rat to obtain a mean value that was compared across groups.

Immunohistochemistry protocols (Fig. 2C, fig. S8)

Microglial and astrocytic reactivity was revealed by performing immunohistological staining against glial fibrillary acidic protein (GFAP) and ionized calcium binding adapter molecule 1 (Iba1), respectively. Briefly, lumbosacral spinal cord coronal sections were incubated overnight in serum containing anti-Iba1 (1:1000, Abcam, USA) or anti-GFAP (1:1000, Dako, USA) antibodies. Immunoreactions were visualized with appropriate secondary antibodies labeled with Alexa fluor® 488 or 555. A fluorescent counterstaining of the Nissl substance was performed with the Neurotrace 640/660 solution (1:50, Invitrogen, USA). Sections were mounted onto microscope slides using anti-fade fluorescent mounting medium and covered with a cover-glass. The tissue sections were observed and photographed with a laser confocal fluorescence microscope (Leica, Germany).

Immunostaining quantification

Immunostaining density was measured offline using 6 representative confocal images of lumbosacral segments per rat. Images were acquired using standard imaging settings that were kept constant across rats. Images were analyzed using custom-written Matlab scripts according to previously described methods (4). Confocal output images were divided into square regions of interest (ROI), and densities computed within each ROI as the ratio of traced fibers (amount of pixels) per ROI area. Files were color-filtered and binarized by means of an intensity threshold. Threshold values were set empirically and maintained across sections, animals and groups. All the analyses were performed blindly.

μ-Computed Tomography

Spinal cord model (Fig 2D, fig. S10)

Non-destructive computed tomography (CT) reconstructions of the spinal cord model were obtained with a Skyscan 1076 scanner (Bruker microCT, Kontich, Belgium). The following settings were used: accelerating voltage 40 kV, accelerating current 250 μA, exposure time per image 180 ms, angular resolution 0.5°. The resultant projection images were reconstructed into 3D renderings of the model using NRecon and GPURecon Server (Bruker microCT, Kontich, Belgium). The resultant volumetric reconstructions had a voxel size of 37μm. This limit prevented the direct visualization of stiff implants, whose thickness was 25μm.

In-vivo implant imaging (Fig. 1F)

Imaging of implanted e-dura (5 weeks post implantation) was conducted in the same scanner. Rats were kept under Isoflurane anesthesia during the scan to reduce motion artifacts. Scanner settings were adjusted to avoid artefacts induced by metallic parts of the spinal orthosis (typical settings were: 1 mm aluminum filter, voltage 100 kV, current 100 μA, exposure time 120 ms, rotation step 0.5). Prior to imaging, a contrast agent (Lopamiro 300, Bracco, Switzerland) was injected through the microfluidic channel of the implants to enable visualization of soft tissues and e-dura. Segmentation and 3D model were constructed with Amira® (FEI Visualization Sciences Group, Burlington, USA).

Recordings and analysis of muscle activity and whole-body kinematics (Fig. 2, Fig. 4, fig. S6, fig. S17, fig. S18)

Bilateral hindlimb kinematics were recorded using 12 infrared motion capture cameras (200 Hz; Vicon). Reflective markers were attached bilaterally overlying iliac crest, greater trochanter (hip), lateral condyle (knee), lateral malleolus (ankle), distal end of the fifth metatarsal (limb endpoint) and the toe (tip). Nexus (Vicon) was used to obtain 3D coordinates of the markers. The body was modeled as an interconnected chain of rigid segments, and joint angles were generated accordingly. Muscle activity signals (2 kHz) were amplified, filtered (10–1000-Hz bandpass) and recorded using the integrated Vicon system. Concurrent video recordings (200 Hz) were obtained using two cameras (Basler Vision Technologies) oriented at 90° and 270° with respect to the direction of locomotion (S10).

A minimum of 8 gait cycles was extracted for each experimental condition and rat. A total of 135 parameters quantifying gait, kinematics, ground reaction force, and muscle activity features were computed for each limb and gait cycle according to methods described in detail previously (S10). These parameters provide a comprehensive quantification of gait patterns ranging from general features of locomotion to fine details of limb motion. The entire list of 135 computed parameters is described in **table S1**.

Principal component analysis

The various experimental conditions led to substantial gait changes, which were evident in the modification of a large proportion of the computed parameters. In order to extract the relevant gait characteristics for each experimental condition, we implemented a multi-step statistical procedure based on principal component (PC) analysis (30). PC analyses were applied on data from all individual gait cycles for all the rats together. Data were analyzed using the correlation method, which adjusts the mean of the data to zero and the standard deviation to 1. This is a conservative procedure that is appropriate for variables that differ in their variance (e.g. kinematic vs. muscle activity data). PC scores we extracted to quantify differences between groups or conditions. Analysis of factor loadings, i.e. correlation between each variable and PC, identified the most relevant parameters to explain differences illustrated on each PC.

Acute recordings of electrocorticograms in mice (Fig. 4A)

Thy1-ChR2-YFP mice were anesthetized with Ketamine/Xylazine and head-fixed in a stereotaxic frame (David Kopf Instruments). A 2x2 mm² craniotomy was performed over the leg area of the motor cortex, which was verified by the induction of leg movements in response to optogenetic stimulation. The e-dura was placed over the exposed motor cortex and covered with physiological saline. We employed a diode-pumped solid state blue laser (473 nm, Laserglow technologies) coupled via a FC/PC terminal connected to a 200µm core optical fiber (ThorLabs) to deliver optical stimulation. Using a micromanipulator, the fiber was placed at the center of each square formed by 4 adjacent electrodes. Optical stimulation was delivered through the transparent elastomeric substrate to illuminate the surface of the motor cortex. A train of light pulses was delivered at 4Hz, 9ms duration, 30mW intensity for each site of stimulation. Electrocorticograms were recorded using the same methods as employed in rats. For each electrode, the amplitude of light-induced electrocorticograms was extracted, normalized to the maximum recorded amplitude for that electrode, and the peak to peak amplitude calculated. The values measured across all the electrodes were used to generate color-coded neuronal activation maps.

Long-term in vivo recordings of electrocorticograms in freely behaving rats (Fig. 4B, fig. S15)

Electrocorticograms were measured in conjunction with whole body kinematics and muscle activity recordings during standing and walking in freely behaving rats (n=3 rats). The rats were tested every week for 3 weeks after chronic implantation of the e-dura over the hindlimb area of the motor cortex. A lateral active site integrated in the e-dura was used as a reference for differential amplification. A wire ground was fixed to the skull using a metallic screw. Differential recordings were obtained using a TDT RZ2 system (Tucker Davis Technologies), amplified with a PZ2 pre-amplifier, sampled at 25 kHz, and digital band-passed filtered (0.1 - 5000 Hz). Raw electrocorticograms were elaborated using previously described methods (28),

which are summarized in **fig. S15**. Kinematic and muscle activity recordings were used to dissociate standing and walking states.

Chronic recordings of electrospinograms (Fig. 4C, fig. S16)

Recordings of electrical potentials from the electrodes integrated in the chronically implanted e-dura, which we called electrospinograms, were performed after 6 weeks of implantation (n=3 rats). Experiments were performed under urethane (1 g/kg, i.p.) anesthesia. Both electrospinograms and muscle activity were recorded in response to stimulation delivered to peripheral nerve or motor cortex. The sciatic nerve was exposed, and insulated from the surrounding tissue using a flexible plastic support. A hook electrode was used to deliver single biphasic pulses of increasing amplitude, ranging from 150 to 350 μ A, and 100 μ s pulse-width, at 0.5 Hz. Each trial was composed of at least 30 pulses. Responses measured in chronically implanted muscles and from each electrode integrated in the e-dura, were extracted and triggered-averaged. To elicit a descending volley, a custom-made wire electrode was inserted overlying the leg area of the motor cortex, in direct contact with the dura mater. Current controlled bi-phasic pulses were delivered every minute using a 1mA, 1ms pulse-width stimulus. Responses were then extracted, and triggered-averaged. Signals were recorded using a TDT RZ2 system (Tucker Davis Technologies), amplified with a PZ2 Pre-amplifier, and sampled at 25 kHz with a digital band-passed filtered (1 - 5000 Hz). Electrospinograms were recorded differentially from each active site of the implants with respect to a reference fixed to one of the bony vertebrae. The latency, amplitude, and amplitude density spectrum of the recorded signals were analyzed offline.

Electrochemical stimulation of the spinal cord (Fig. 4E, fig. S17)

Electrochemical stimulation protocols were selected based on an extensive amount of previous studies in rats with spinal cord injury (4, 29, 30). The chemical stimulation used during training was administered through the microfluidic channel integrated in the chronically implanted e-dura. After 1-2 minutes, subdural electrical stimulation currents were delivered between active electrodes located on the lateral aspect or midline of sacral (S1) and lumbar (L2) segments, and an indifferent ground located subcutaneously. The intensity of electrical spinal cord stimulation was tuned (40Hz, 20-150 μ A, biphasic rectangular pulses, 0.2ms duration) to obtain optimal stepping visually. To demonstrate the synergy between chemical and electrical stimulation, we tested rats without any stimulation, with chemical or electrical stimulation alone, and with concurrent electrochemical stimulation. To demonstrate the previously inaccessible capacity to facilitate specific aspects of locomotion with subdural electrical stimulation, we delivered electrical stimulation using electrodes located on the lateral aspects of lumbar and sacral segments, and compared locomotor movements with stimulation delivered bilaterally.

Statistical analysis

All the displayed quantifications are reported as mean values \pm SEM (standard error of mean), unless otherwise stated. Statistical evaluations were performed using paired Student's t-test, one-way analysis of variance (ANOVA), repeated-measure ANOVA or Friedman test, depending on the experimental design. In case of limited number of measurements, we used their non-parametric equivalents: Wilcoxon ranksum test and Kruskal-Wallis one-way analysis of variance. The Tukey's range test and Bonferroni procedure were applied to test post-hoc differences when appropriate.

Supplementary text:

Deformation analysis of the spinal cord - implant model (fig. S10)

The biomechanical coupling of the implant with the spinal cord depends on the implant's materials and geometry, and the mechanical response of the spinal cord.

Influence of implant bending stiffness

Bending stiffness is defined by Eq. 1,

$$D = \frac{Et^3}{12(1-\nu^2)} \quad (1)$$

where E and ν are Young's modulus and Poisson's ratio of the implant material, respectively, and t is the thickness of the implant. We neglected the contribution of the thin metal interconnects on the overall implant mechanical behavior.

If the bending stiffness of the implant is large compared to that of the surrounding tissue, the implant cannot accommodate the deformation of the tissue. In the context of an implant inserted in the intrathecal space, this translates in compression of the spinal tissue. We used plane strain finite element simulation to investigate the effect of bending stiffness of the implant on the deformation of spinal tissues and quantified the resulting maximum principal logarithmic strain inside the hydrogel 'spinal tissue'. When the bending stiffness of the implant is much higher than that of dura mater, the implant distorts the spinal tissue. The lower the bending stiffness, the less interference is induced by the implant. Ideally the bending stiffness of the implant should be as low as possible. In practice, bending stiffness comparable to dura mater may be sufficient, as demonstrated with results obtained with the soft e-dura implants.

Influence of tensile stiffness mismatch (fig. S10C)

Tensile stiffness is defined in Eq. 2:

$$S = EA \quad (2)$$

with A , the cross-sectional area of the structure perpendicular to the tensile/compression direction and E , the Young's modulus of the implant material.

We define three zones along the length of the spinal cord model: in zone 1, the spinal tissue is implant-free, in zone 2, the implant sits above the spinal tissues, and zones 3 depict the transition between zones 1 and 2.

Except for the transition region of the size comparable to the diameter of the spinal cord, the strain of the regions 1 and 2 should be homogeneous. By force balance we will have:

$$S_1\varepsilon_1 = S_2\varepsilon_2 \quad (3)$$

with ε_1 and ε_2 the strain in zone 1 and 2 respectively.

If the implant is very stiff, then $S_1 \gg S_2$. As a result, $\varepsilon_1 \ll \varepsilon_2$ and the implant will severely limit the motion of the spinal tissue.

A stiff implant may also result in debonding during stretch. The debonded implant will slide relative to the spinal cord and dura mater as the animal moves. Such repetitive relative movements may trigger and maintain neuroinflammation in the spinal tissue. The energy release rate G for debonding is expressed in Eq. 4:

$$G = \frac{S_2 \varepsilon_2^2}{2w} - \frac{S_1 \varepsilon_1^2}{2w} \quad (4)$$

where w is the bonding width of the implant (25).

When an overall strain ε_{app} is applied along the spinal cord system,

$$l\varepsilon_{app} = l_1\varepsilon_1 + l_2\varepsilon_2 \quad (5)$$

Once the implant material and geometry are selected, $\varepsilon_1, \varepsilon_2$ and G can be resolved with equations (3)-(4)-(5). The table below summarizes these parameters when the spinal cord-implant model is stretched by 10% strain, and compares the different coverage rate of the implant, characterized by the ratio l_1/l , for the soft (PDMS) and stiff (polyimide) implants. Two thicknesses of polyimide implants are simulated (25 μ m and 2.5 μ m). The bending stiffness of an extremely thin (2.5 μ m) polyimide is negligible compared to that of a 25 μ m thick polyimide film (fig. S10).

	120 μ m PDMS ($S_1/S_2 = 1.33$)			25 μ m Polyimide ($S_1/S_2 = 88.13$)			2.5 μ m Polyimide ($S_1/S_2 = 9.71$)		
l_1/l	ε_1	ε_2	G	ε_1	ε_2	G	ε_1	ε_2	G
10%	7.7%	10.3%	1.0J/m ²	0.1%	11.0%	4.4J/m ²	0.1%	11.0%	3.9J/m ²
50%	8.6%	11.4%	1.2J/m ²	0.2%	19.8%	13.9J/m ²	0.2%	18.1%	10.6J/m ²
90%	9.7%	12.9%	1.5J/m ²	1.0%	90.7%	291.9J/m ²	5.0%	51.9%	86.7J/m ²

A stiff implant, even extremely thin, severely constraints the motion of the underlying spinal tissues ($0.1\% < \varepsilon_1 < 1\%$ for $\varepsilon_{appl} = 10\%$). Furthermore, as the coverage rate increases, the strain in zone 2 (outside of the implant coverage) is rapidly increasing reaching 50% (2.5 μ m thick implant) and 90% (25 μ m thick implant) (for $\varepsilon_{appl} = 10\%$) when the implant covers 90% of the length of the spinal cord. As the result of this strain concentration, the energy release rate for debonding is one order of magnitude higher than a soft e-dura implant made of PDMS.

Movie S1: Electronic dura mater.

This movie illustrates the resilience of the e-dura under various conditions, and shows a 3D rendering of a computed tomography scan of the e-dura inserted in the spinal subdural space of a rat.

Movie S2: e-dura bio-integration.

This movie shows leg kinematics during locomotion along a horizontal ladder for a sham-operated rat, a rat implanted with the e-dura and a rat implanted with a stiff implant, and a 3D rendering of the reconstructed spinal cords after 6 weeks of implantation.

Movie S3: e-dura applications.

This movie shows leg kinematics during bipedal locomotion on a treadmill under various combinations of chemical and electrical stimulation of lumbosacral segments for a rat that received a severe spinal cord injury leading to permanent paralysis.

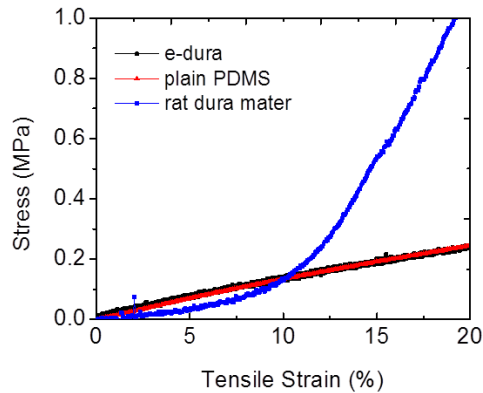


Figure S1. Tensile response of natural dura mater, silicone and e-dura implant.

Stress-strain curves of explanted rat dura mater, e-dura and plain membrane of silicone (PDMS). Both e-dura (120 μ m thick) and the plain silicone membrane (85 μ m thick) are linearly elastic in the tested strain range and poses similar elastic moduli of approximately 1.2MPa. Freshly explanted spinal rat dura exhibits a 'J' shaped stress-strain curve typical of collagen rich biomaterials. At elongations up to approximately 10%, natural rat dura and e-dura exhibit similar tensile properties. Strain rate is 0.5%/s.

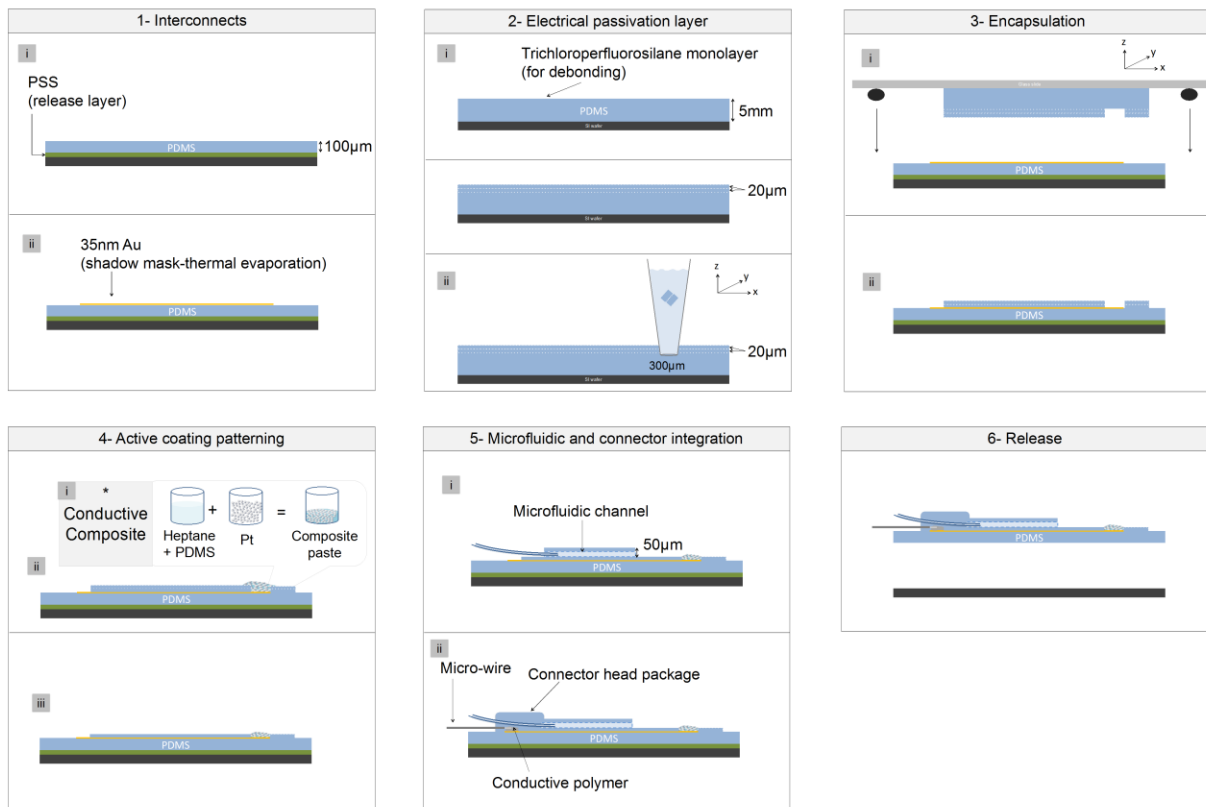


Figure S2. Soft neurotechnology for e-dura implants.

The process flow, illustrated in cross-sectional views, consists of 6 main steps. (1) Elastomeric substrate and stretchable interconnects fabrication. Patterning (2) and bonding (3) of interconnects' passivation layer. (4) Coating of the electrodes with a customized platinum-silicone composite screen-printed above the electrode sites. (5) Integration of the PDMS microfluidic channel and connector. (6) Release of the e-dura implant in water.

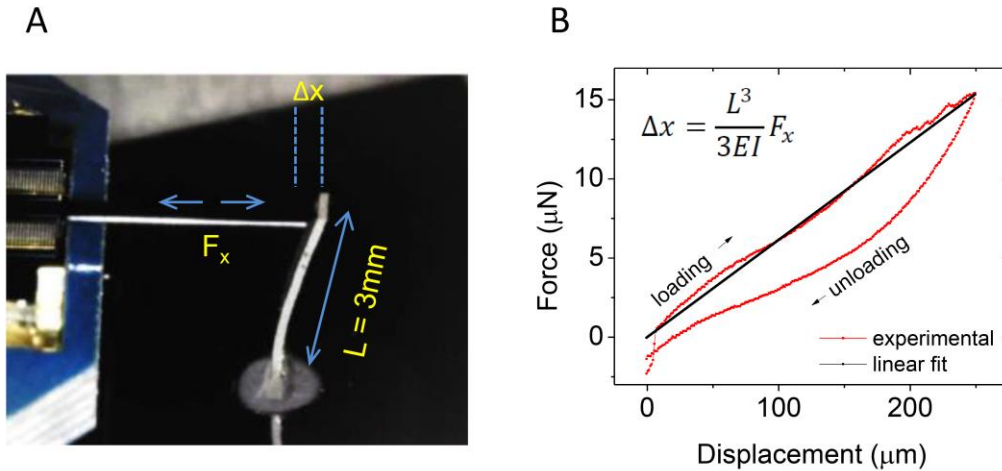


Figure S3. Mechanical characterization of the platinum-silicone composite.

(A) To estimate the elastic modulus of the coating composite, we fabricated a high aspect ratio pillar with a rectangular cross-section ($L = 3 \text{ mm}$, $h = 113 \text{ }\mu\text{m}$, $w = 480 \text{ }\mu\text{m}$, 4:1 w:w Pt:PDMS composite). The pillar was then mounted vertically. (B) To obtain a force-displacement curve, we measured the force required to deflect the free end of the pillar by a small distance Δx . We used a linear fit to the loading portion of the force-displacement curve and bending beam theory to derive the Young's Modulus (E) of the composite. In this equation, I is the moment of inertia defined by the known cross-section dimensions of the beam, E is the elastic modulus of the beam, and F_x is the force needed to produce a displacement Δx . We found the elastic modulus of the platinum-silicone composite was approximately 10 MPa.

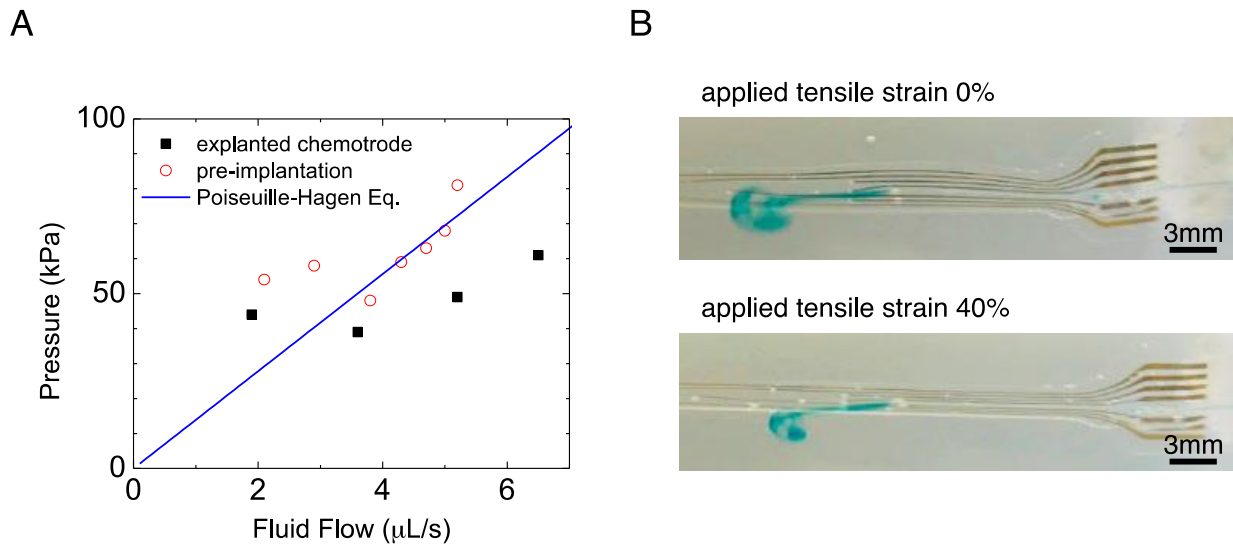


Figure S4. e-dura chemotrode: compliant fluidic microchannel.

(A) Determination of the hydrodynamic resistance of the microfluidic system. The continuous line displays the fluid flow predicted by the Poiseuille-Hagen equation. Monitoring the hydrodynamic response of the chemotrode before surgery and after explantation following 6 weeks of chronic implantation demonstrated that the microfluidic channels do not become occluded with tissue or debris, and maintain functionality during prolonged subdural implantation. (B) Blue-colored water was injected through the chemotrode under different tensile conditions. The integrity and functionality of the microfluidic channel was maintained when the implants was stretched up to a strain of 40%.

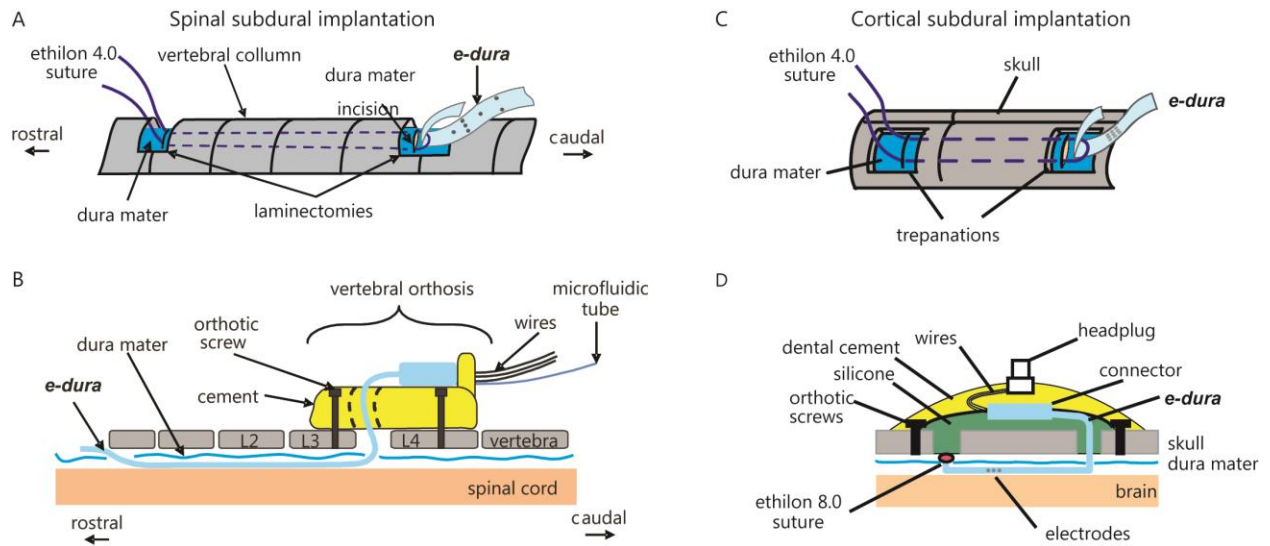


Figure S5. Orthoses and surgical procedures for chronic e-dura implantation.

(A-B) Spinal e-dura. (A) Surgical procedure to slide the e-dura below the dura mater covering lumbar segments. (B) Side view of the engineered vertebral orthosis that secures the e-dura connector, and ensures long-term functionality of embedded electrodes and chemotrode in vivo. (C-D) Cortical e-dura. (C) Surgical procedure to slide the e-dura below the dura mater covering the motor cortex. (D) Side view describing the engineered cortical orthosis that secures the e-dura and its connector, ensuring chronic recordings of electrocorticograms in freely moving rats.

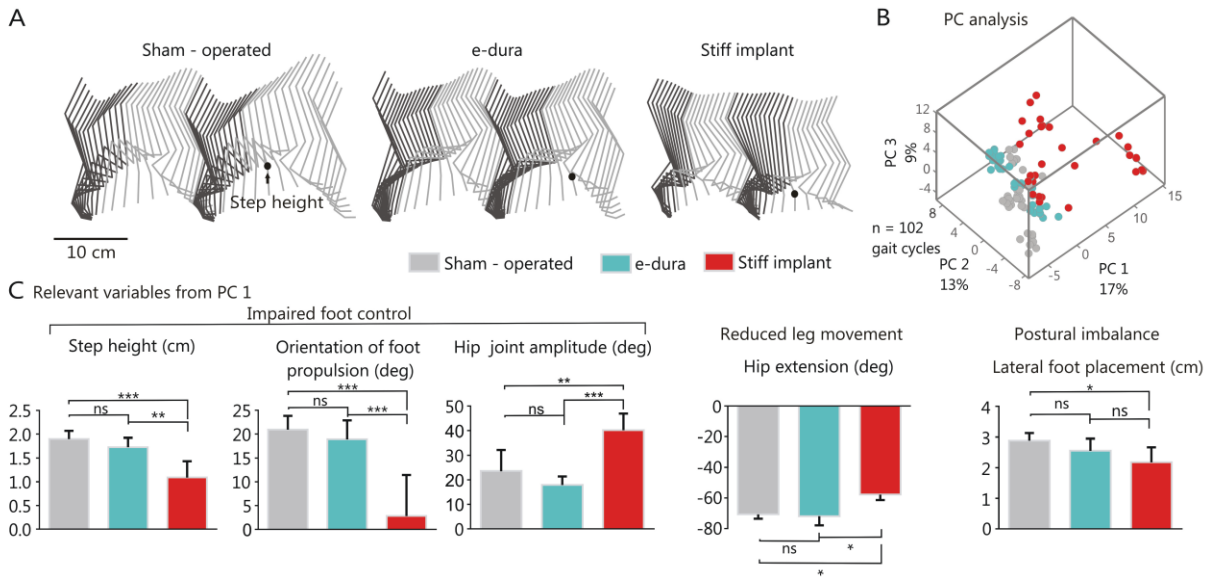


Figure S6. Kinematic analysis of gait patterns during basic overground locomotion.

(A) Representative stick diagram decomposition of hindlimb movement during two successive gait cycles performed along a horizontal unobstructed runway. Recordings were obtained 6 weeks after surgery for a sham-implant rat, and for a rat implanted with an e-dura or a stiff implant, from left to right. (B) A total of 135 parameters providing comprehensive gait quantification (Table S1) were computed from high-resolution kinematic recordings. All the parameters computed for a minimum of 8 gait cycles per rat at 6 weeks post-implantation were subjected to a principal component (PC) analysis. All gait cycles ($n = 102$, individual dots) from all tested rats ($n = 4$ per group) are represented in the new 3D space created by PC1-3, which explained 40% of the total data variance. This analysis revealed that sham-operated rats and rats with e-dura exhibited similar gait patterns, whereas rats with stiff implants showed markedly different gait characteristics compared to both other groups. (C) To identify the specific features underlying these differences, we extracted the parameters with high factor loadings on PC1, and regrouped them into functional clusters (not shown), which we named for clarity. This analysis revealed that rats with stiff implants displayed impaired foot control, reduced amplitude of leg movement, and postural imbalance. To illustrate these deficits using more classic parameters, we generated plots reporting mean values (\pm SEM) of variables with high factor loadings for each of the 3 identified functional clusters. Statistical test: Kruskal-Wallis ANOVA. ***, $P < 0.001$. **, $P < 0.01$. *, $P < 0.05$. ns, non-significant. Error bars: standard error of mean, SEM.

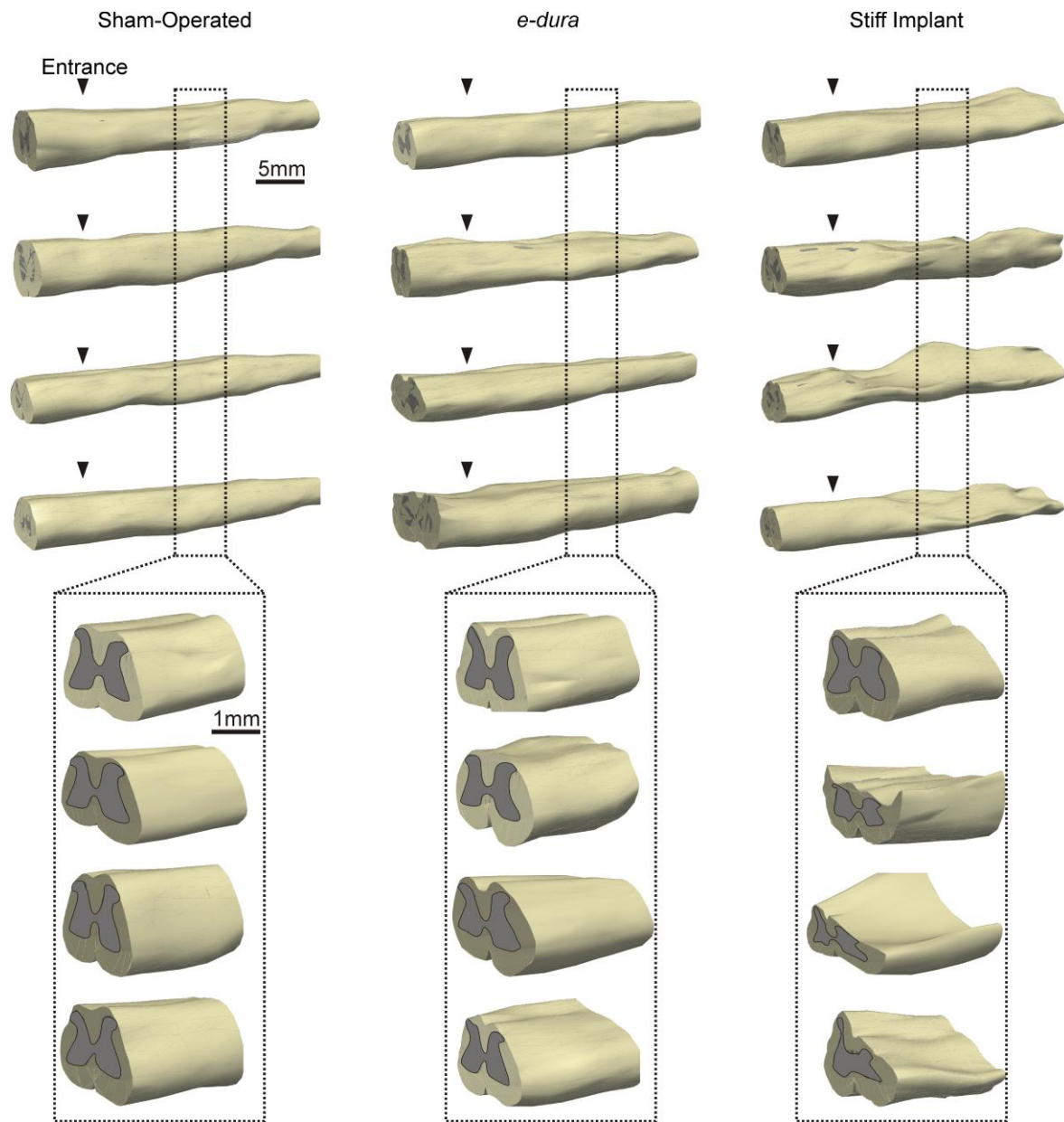


Figure S7. Damage of spinal tissues after chronic implantation of stiff, but not soft, implants.

3D reconstructions of lumbar segments for all 16 tested rats (3 groups of 4 animals), including enhanced views. The spinal cords were explanted and reconstructed through serial Nissl-stained cross-sections after 6-week implantation. Stiff implants induced dramatic damage of neural tissues, whereas the soft implant had a negligible impact on the macroscopic shape of the spinal cord. The arrowheads indicate the position of the entrance of the implant into the subdural space.

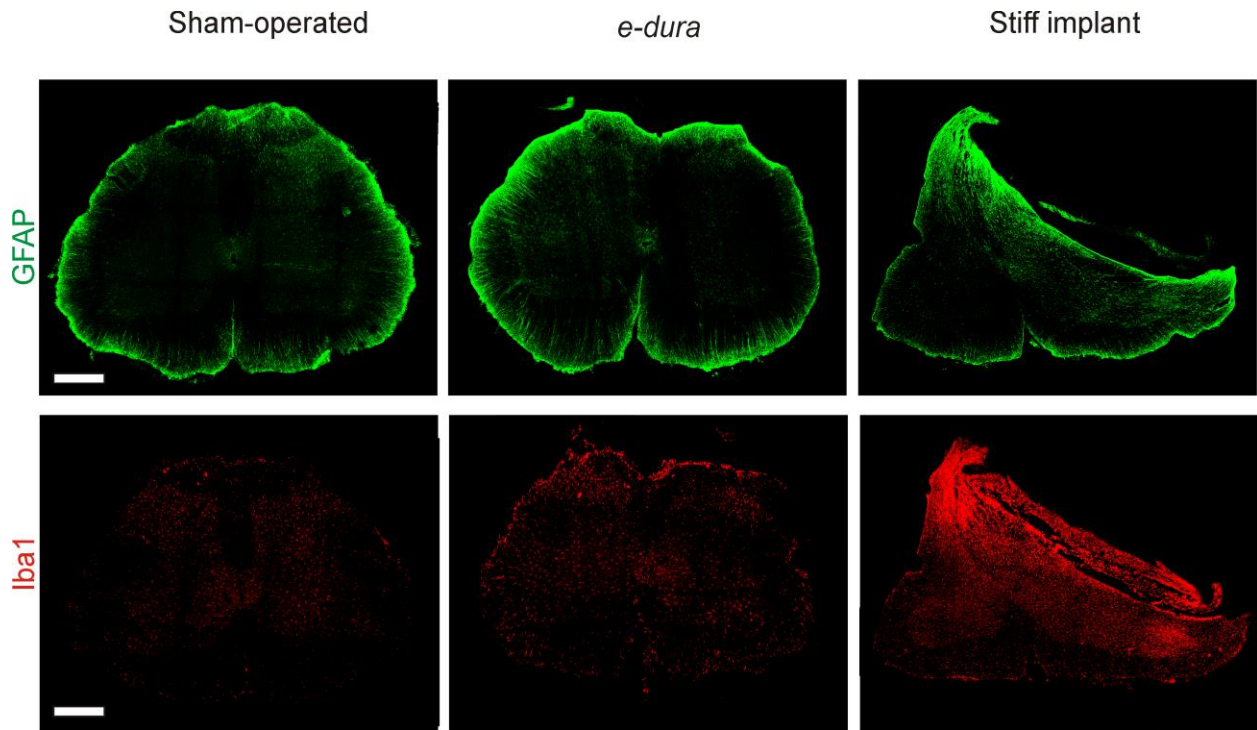


Figure S8. Significant neuro-inflammatory responses after chronic implantation of stiff, but not soft, implants.

Cross-section of the L5 lumbar segment stained for the neuro-inflammatory markers GFAP (astrocytes) and Iba1 (microglia) after 6-week implantation. A representative photograph is shown for each group of rats. The stiff implant leads to a dramatic increase in the density of neuro-inflammatory cells, whereas the *e-dura* had a negligible impact on these responses. Scale bars, 500 μ m.

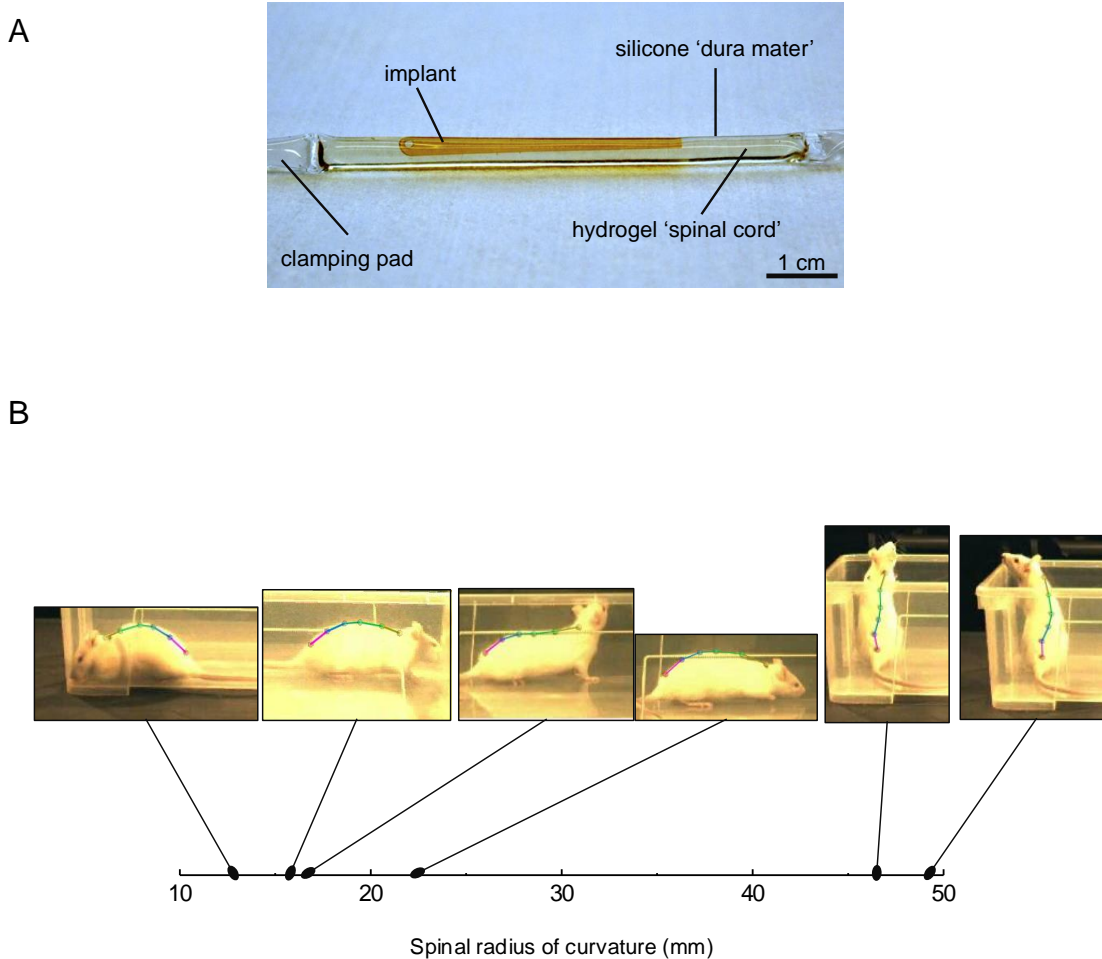


Figure S9. Model of spinal cord and experimental quantification of vertebral column curvatures in freely behaving rats.

(A) The mechanical model of spinal cord is composed of a hydrogel that simulates spinal tissue, and a silicone membrane that simulates the dura mater. The soft or stiff implant was inserted between the hydrogel and the silicone membrane. The water trapped under the simulated dura mater ensured constant lubrication of the entire implant. Both ends of the model were sealed with silicone forming the clamping pads used in stretching experiments. (B) To measure the range of physiologically relevant vertebral column curvatures, we recorded spontaneous movement of a healthy rat during exploration of a novel environment. Reflective markers were attached overlying bony landmarks to measure motion of the vertebral column. The photographs displayed the stereotypical motor behaviors that were extracted for further analysis. For each behavior, we fitted a polynomial function through the inter-connected chain of markers. The resulting curvatures are reported along the x-axis. Since the markers were attached to the moving skin, the radii of curvature experienced by the vertebral column, and even more by the spinal cord itself, are expected to be at least 1 to 2mm smaller. We used the measured radii of curvature to define the bending limits applied to the spinal cord-implant model tested under flexion.

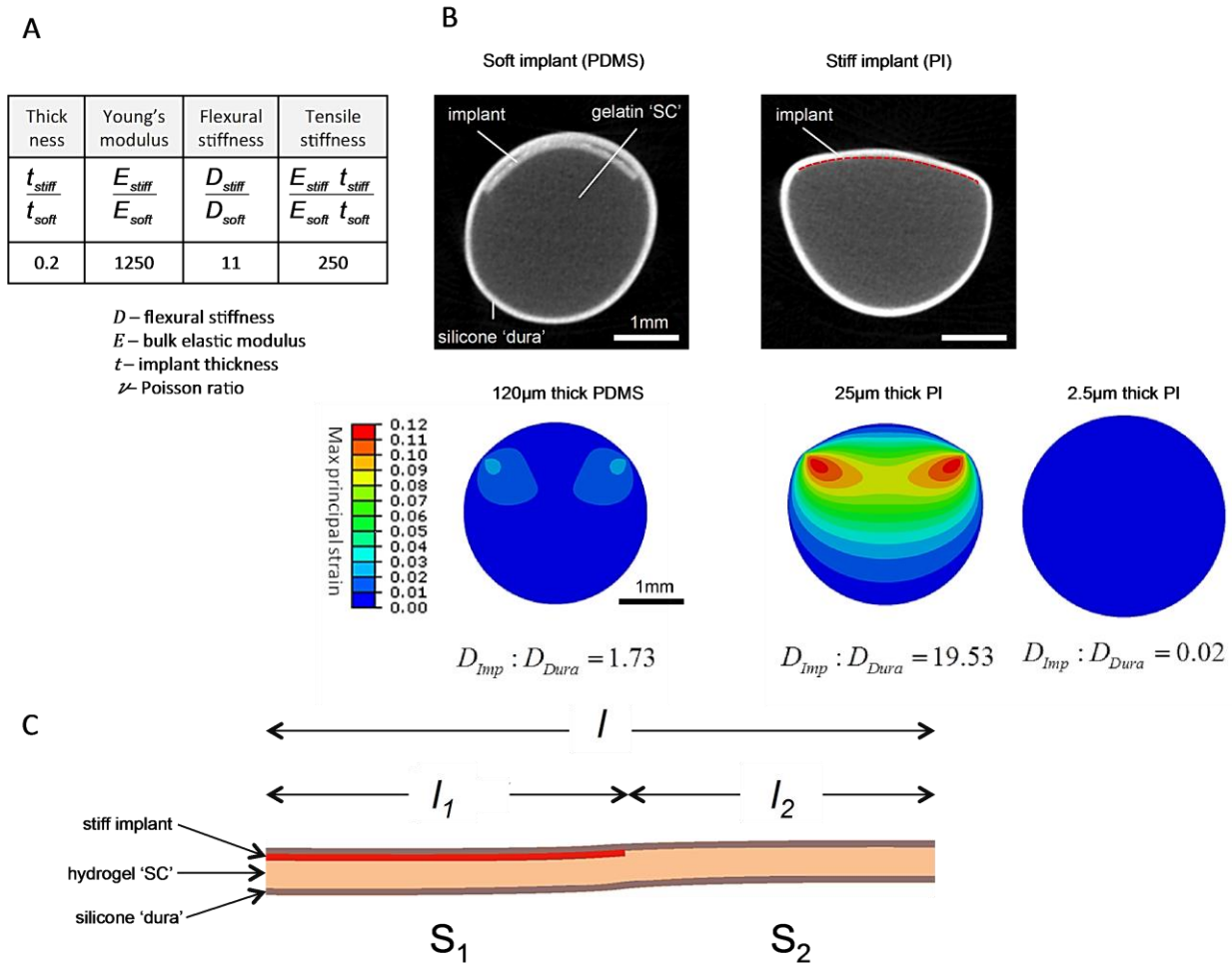


Figure S10. Mechanical effects of implants on the model of spinal cord.

(A) Ratios of the mechanical properties of the materials used to prepare the soft (i.e. silicone) and stiff (i.e. polyimide) implants. Bending stiffness describes the resistance of the implant towards flexion, while tensile stiffness refers to the resistance of the implant towards elongation. Although the stiff implant is five times thinner than the soft implant, its tensile and flexural stiffness are respectively two and one orders of magnitude larger. (B) Micro-Computed Tomography (μ CT) images and Finite Element (FE) Simulation strain maps of the cross-sections of the model of spinal cord carrying a soft or a stiff implant. No external deformation is applied to the model. The 25 μ m thick polyimide implant is highlighted with a dotted red line because the resolution of the μ CT is not high enough to distinguish the thin plastic film. The FE simulations depict the maximum logarithmic strain inside the model of spinal cord computed with the geometry and materials properties of the spinal cord models and three implant configurations (120 μ m soft PDMS, 25 μ m and 2.5 μ m thick polyimide films). (C) Schematic longitudinal cross-section of the model of spinal cord model carrying a stiff implant. The model system is stretched along the length of the implant by 20% strain. The high tensile stiffness $S_{stiff} = E_{stiff} \cdot t_{stiff}$ of the implant compared to that of the simulated spinal cord leads to nearly

unstretched simulated spinal tissues immediately underneath the implant and highly deformed spinal tissues away from the implant.

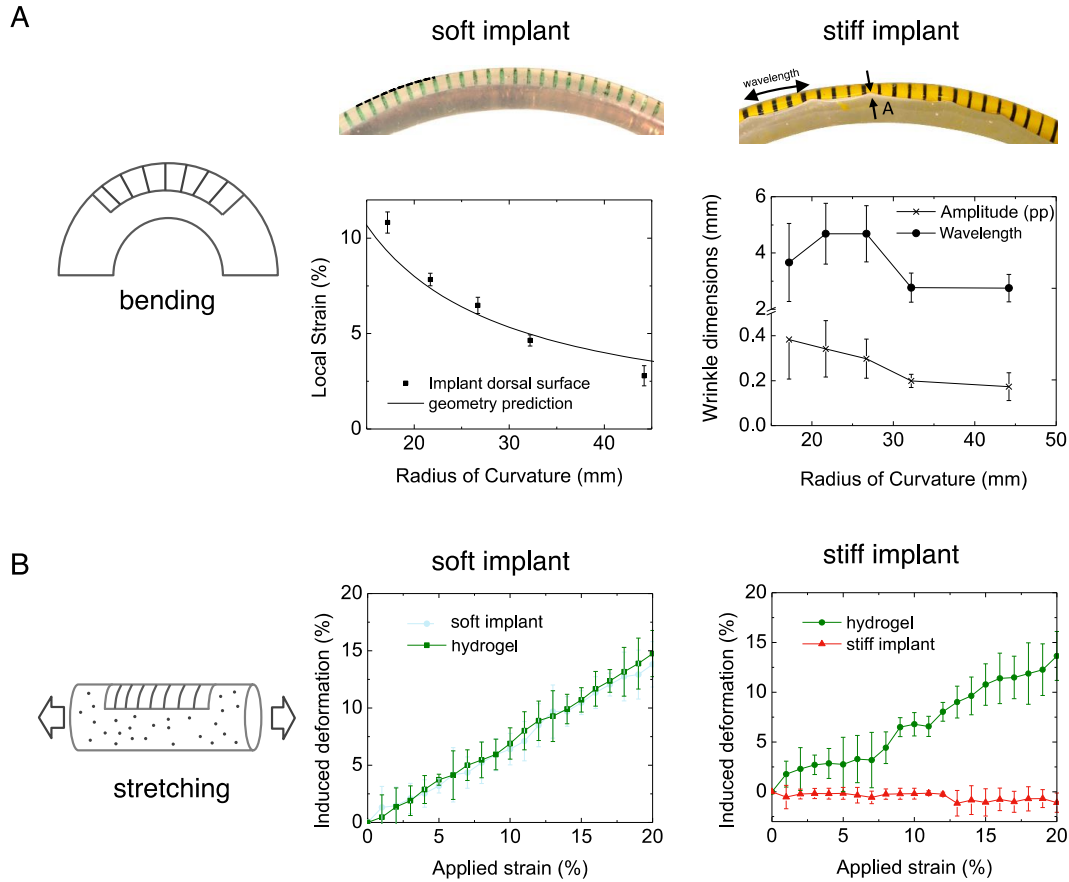


Figure S11. Effect of tensile deformations on the implants and on the model of spinal cord.

(A) To measure local strains, we tracked fiducial markers in the hydrogel ‘spinal tissue’ and on the soft or stiff implant. Graphite powder particles were mixed with the hydrogel during gel preparation. Parallel lines with 1mm inter-distance were drawn directly onto the surface of the implants. The model was flexed to controlled bending radii, which covered the entire range of physiologically relevant spinal movement determined in vivo (**fig. S9**). The soft implant conformed to the flexion of simulated spinal tissues. The strain along the sagittal crest of the model (broken line) was determined experimentally (discrete symbols) and compared to a geometrical prediction (continuous line). The stiff implant started wrinkling with radii smaller than 30mm. The amplitude of wrinkles, termed A, and the wavelength depended on the bending radius. (B) The spinal cord - implant model was placed under uniaxial (global) tensile stretch. Local strain was measured by tracking the displacement of pairs of particles in the gel (n=8 pairs), or neighboring stripes on the implants (n=10 pairs). The graphs quantify locally induced strain in the implant and in the hydrogel core (spinal tissues) as a function of the global applied strain to the model. The soft implant stretched with the model of spinal cord. In contrast, there was a substantial mismatch between the local strain inside the model and the induced deformation of the stiff implant. Consequently, the stiff implant slid between the silicone and the hydrogel during stretch. Mean \pm standard deviation (SD).

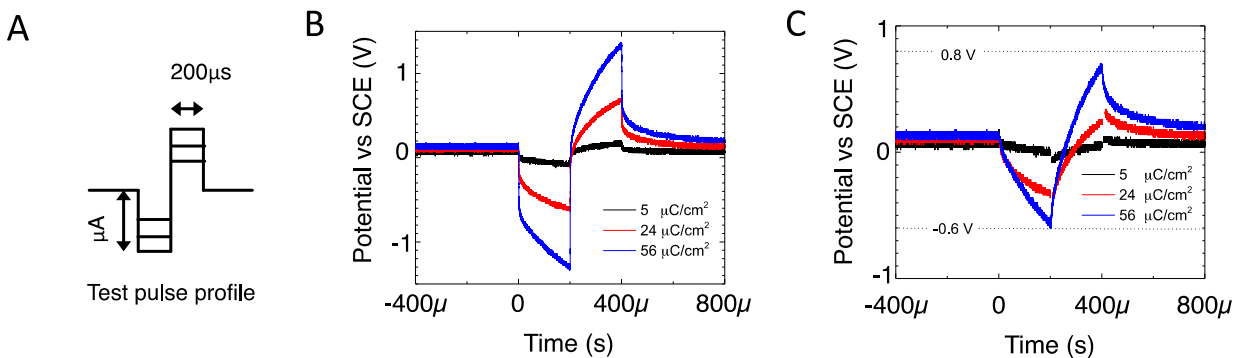


Figure S12. Determination of charge injection capacity of electrodes with platinum-silicone coating.

(A) Charge-balanced, biphasic current pulses were injected through electrodes immersed in Phosphate Buffer Saline solution (PBS). The duration of each pulse phase was fixed at 200 μs per phase, which corresponds to the typical pulse duration used during therapeutic applications. (B) The amplitude of the current pulses was gradually increased. As the current density flowing through the coating and its polarization increased, a significant portion of the recorded voltage drop occurred in the electrode interconnects and the electrolyte above the coating. (C) To obtain the true voltage transients at the coating surface with respect to the reference electrode, the instantaneous polarization of the cell was subtracted. The maximum safe current density was reached when the coating polarization exited the water window.

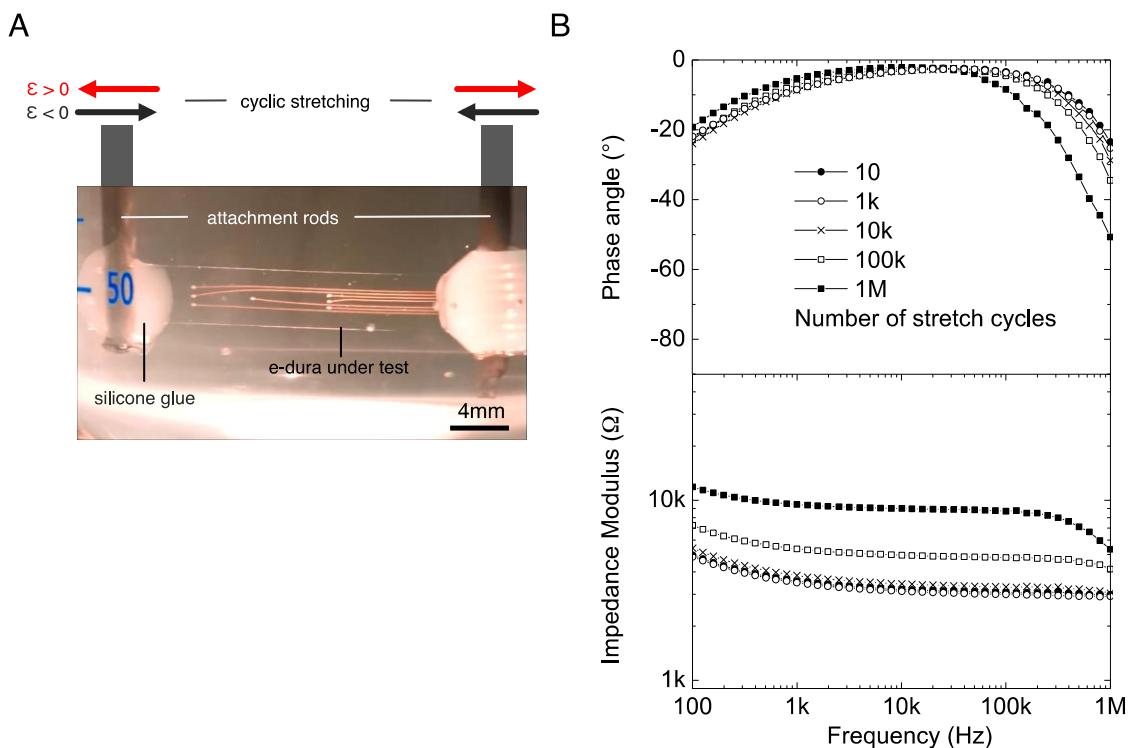


Figure S13. Impedance spectroscopy of the soft electrodes under cyclic stretching to 20% strain.

(A) Apparatus for conducting electrochemical characterization of soft implants under tensile strain. The ends of the implant were glued to two probes that are clamped to the jaws of a custom built extensimeter. The implant and (partially) the probes were then submerged in Phosphate Buffered Saline solution (PBS). The extensimeter applied pre-defined static strain to the implant, or performed a cyclic stretch-relax program. A counter and a reference electrode were submerged in the electrolyte to complete the circuit (not shown). (B) Representative impedance plots recorded from one electrode. The spectra were recorded at 0% applied strain after 10, 1,000, 10,000, 100,000 and 1 million stretch cycles. Each stretch cycle lasted 1s. The implants remained immersed in PBS throughout the evaluations. The remaining 6 electrodes in the tested implants exhibited a similar behavior.

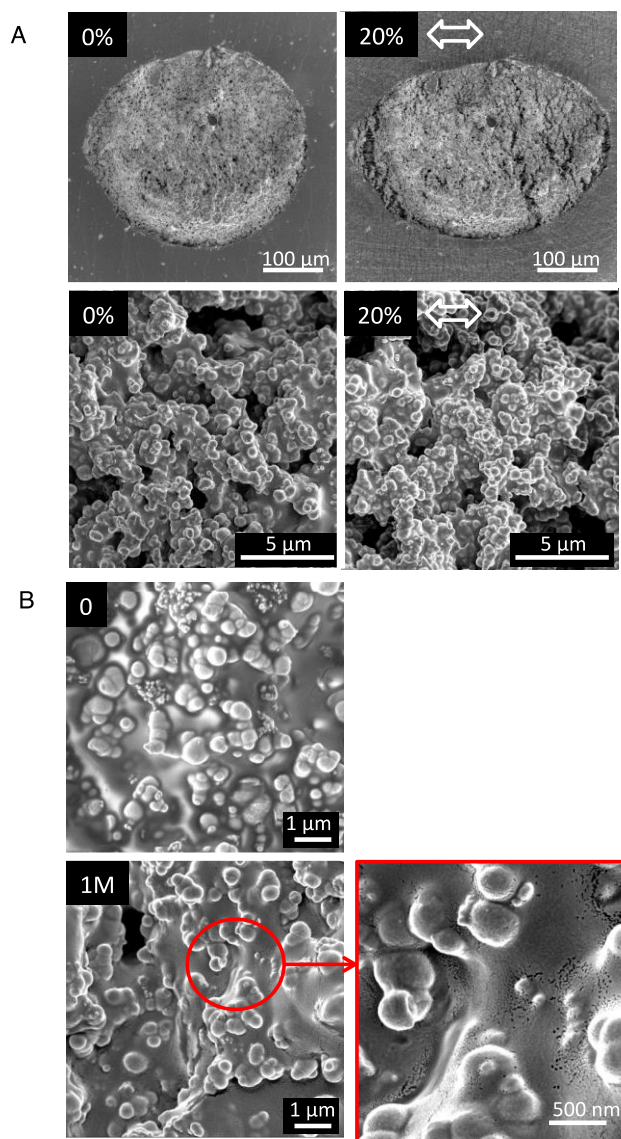


Figure S14. In-situ scanning electron micrographs of platinum-silicone coatings.

(A) Images collected during the first stretch cycle to 20% applied strain (from pristine electrode). Low magnification scanning electron micrographs taken at 20% strain revealed the appearance of cracks, but the absence of delamination. The high effective surface area of the composite coating is clearly visible in medium magnification scanning electron micrographs (lower panels). (B) Images collected before (cycle 0) and after one million stretch cycles to 20% strain. All the images were taken at 0% strain. High-magnification scanning electron micrographs revealed the effects of fatigue cycling on the nano-scale morphology of the composite coating.

standing and walking states. To calculate the time-resolved power of electrocorticograms within each contiguous band, we integrated the electrode-averaged trPSD across that band. We then compared all time-resolved power measurements during walking periods against all time-resolved power measurements during standing periods for each band using Wilcoxon rank-sum test. The low (LFB) and high (HFB) frequency bands (shared areas) were identified as bands with the local minima of p values. Histogram plots report the mean values \pm SEM of electrode-averaged power in the identified bands. ***, $p < 0.001$. p value corrected for multiple comparisons using Bonferroni correction ($n_{\text{tests}} = 45,150$ for each rat). **(E)** Electrode-averaged trPSD, identified low and high frequency bands, and histogram plots reporting means \pm SEM of power in identified bands for walking and standing states, are shown for each rat ($n = 3$ rats in total). Elevated power in low and high frequency bands during walking compared to standing is consistent with electrocorticogram recordings during hand movements in humans (28).

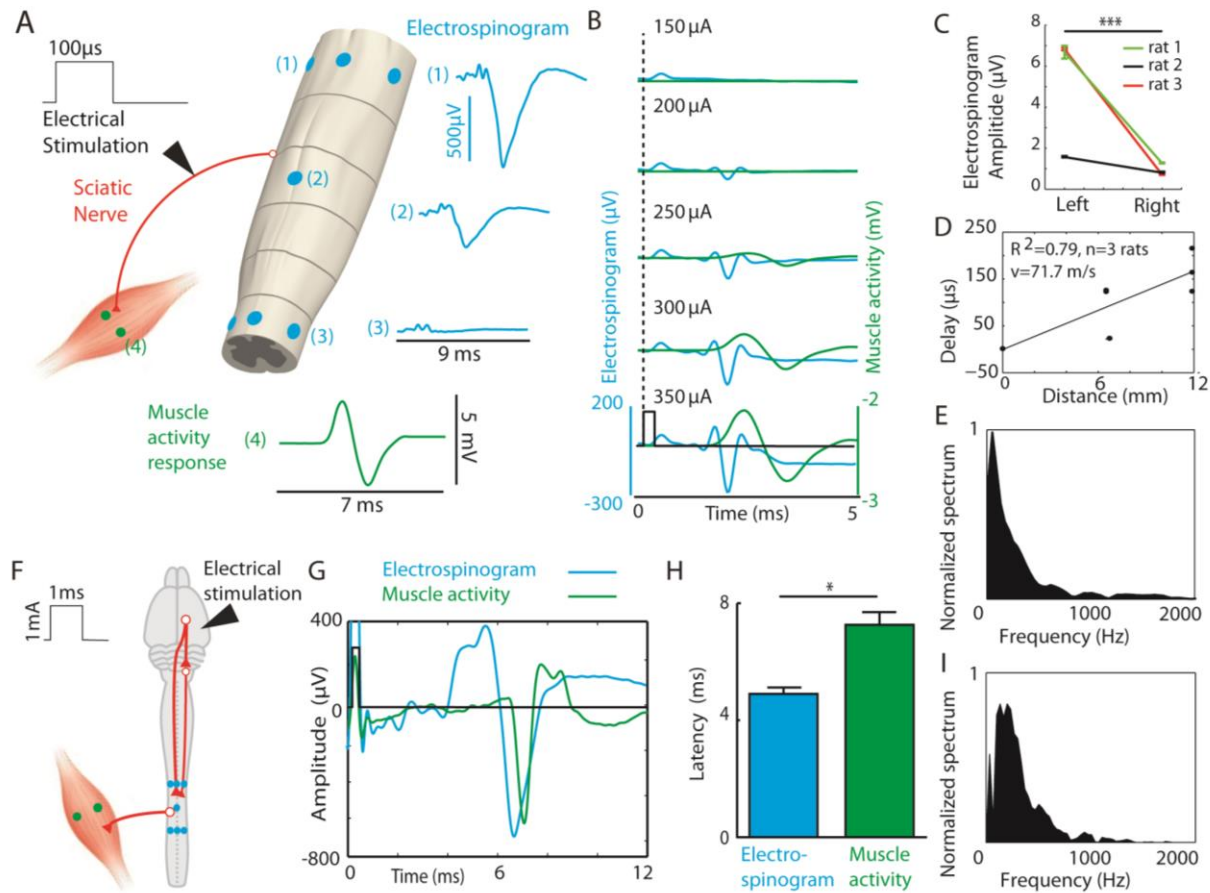


Figure S16. Recordings of electrospinograms following peripheral nerve and brain stimulation.

An e-dura was chronically implanted over lumbar segments for 6 weeks in 3 rats. Terminal experiments were performed under urethane anesthesia. **(A)** Electrospinograms and left medial gastrocnemius muscle activity were recorded in response to electrical stimulation of the left sciatic nerve. **(B)** Representative color-coded electrospinograms and muscle activity responses are displayed for increasing stimulation intensities. Electrospinograms appeared at lower threshold than muscle responses, suggesting that e-dura electrodes measured neural activity related to the recruitment of myelinated fibers. **(C)** Electrospinogram mean amplitudes for left versus right side electrodes (10 trials per rat). Responses were significantly larger on the stimulation side (t-test, ***, $P < 0.001$). **(D)** Correlation plot showing the relationship between electrode location and the latency of electrospinogram responses. The locations are referred to the left L2 electrode, which is the closest to sciatic nerve afferent neurons. The measured neural conduction velocity from lumbar to sacral segments, which was derived from the correlation line, is coherent with the conduction velocity of large-myelinated fibers. **(E)** Power spectrum of electrospinograms is condensed in the region below 1,000Hz, which is consistent with a lead field potential signal, most likely arising from the afferent volley and related synaptic events. These combined results demonstrate the high degree of spatial and temporal selectivity in the

neural recordings obtained with e-dura. **(F)** A stimulating electrode was positioned over the motor cortex of the same rats ($n = 3$) to elicit a descending volley. **(G)** Representative color-coded recording of an electrospinogram and muscle activity following a single pulse of motor cortex stimulation. **(H)** Bar plot reporting the mean (10 trials per rat) latency (\pm SEM) of electrospinograms and muscle activity responses following a single pulse of stimulation. Electrospinograms systematically preceded muscle evoked responses (t-test, *, $P < 0.05$). **(I)** The power spectrum of electrospinograms was condensed in the region below 1,000Hz, which was consistent with a neural response related to multiple descending pathways.

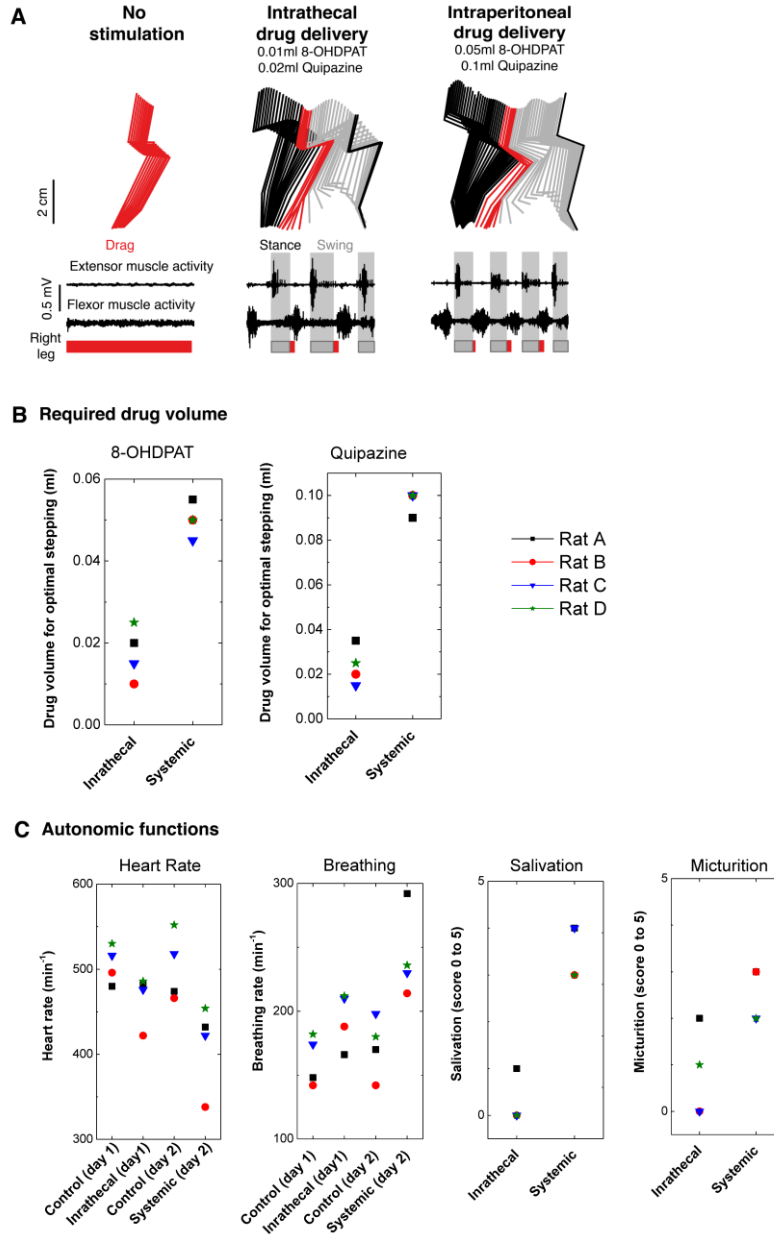


Figure S17. Drug delivery through the chemotrode annihilates side effects.

(A) Rats ($n = 4$) were tested during bipedal locomotion under robotic support after 1 week of rehabilitation. Recordings were performed without stimulation, and with concurrent electrochemical stimulation. Chemical stimulation was delivered either intrathecally through the chemotrode, or intraperitoneally. The drug volumes were adjusted to obtain the same quality of stepping. Color-coded stick diagram decompositions of hindlimb movements are shown together with muscle activity of antagonist ankle muscles. (B) Drug volumes required to obtain optimal facilitation of locomotion for each serotonergic agonist. ($n = 4$ rats). (C) Effects of optimal drug volumes on autonomic functions. Salivation and micturition are reported using a visual scaling system ranging from 0 (baseline, no drug) to 5 (maximum possible effects). ($n = 4$ rats).

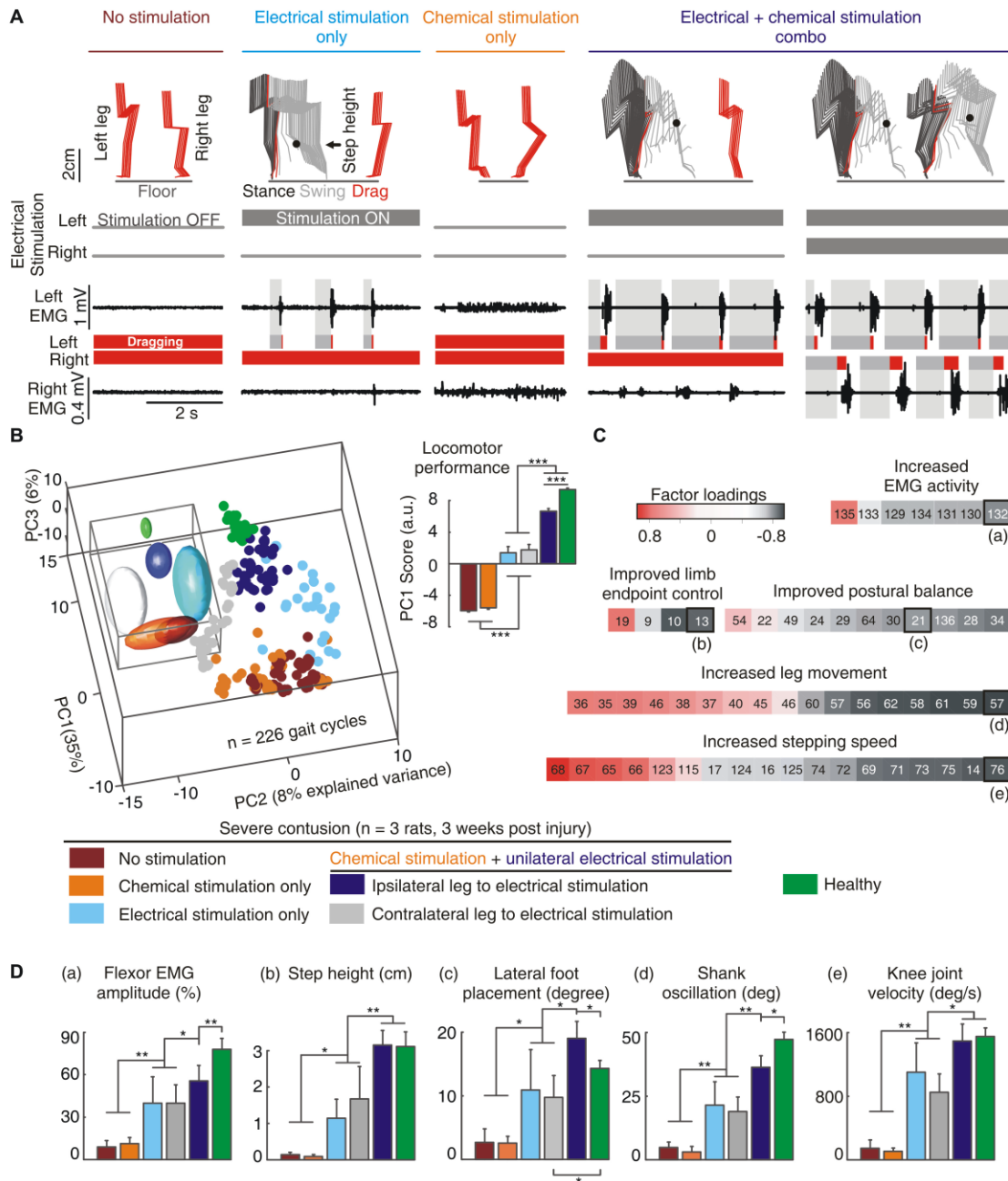


Figure S18. The electrochemical neuroprosthesis e-dura mediates specific adjustments of locomotion.

(A) Spinal cord injured rats (n = 3) were recorded during bipedal locomotion on a treadmill after 3 weeks of rehabilitation. The rats were tested without stimulation (spontaneous) and during various combinations of chemical and/or electrical lumbosacral stimulations, as explained at the top and bottom of each panel. For each condition, a color-coded stick diagram decomposition of left and right hindlimb movements is displayed together with left and right muscle activity, and

the color-coded duration of stance, swing, and drag phases. Without stimulation, both legs dragged along the treadmill belt. Electrical stimulation alone delivered at the level of lumbar (L2) and sacral (S1) electrodes, but only on the left side, induced rhythmic movement restricted to the left leg. Chemical stimulation alone, composed of 5HT_{1A/7} and 5HT₂ agonists, did not induce locomotion, but raised the level of tonic muscle activity in both legs. After chemical injection, delivery of electrical stimulation on the left side induced robust locomotor movements restricted to the left leg. The combination of chemical and bilateral electrical stimulation promoted coordinated locomotor movements with weight bearing, plantar placement, and alternation of left and right leg oscillations. **(B)** A total of 135 parameters providing comprehensive gait quantification (**Table S1**) was computed from kinematic, kinetic, and muscle activity recordings. All the parameters were subjected to a PC analysis, as described in **fig. S6**. All the gait cycles (n = 226, individual dots) from all the tested rats (n = 3) and 3 healthy rats are represented in the new 3D space created by PC1-3, which explained nearly 50% of the total data variance. The inset shows elliptic fitting applied on 3D clusters to emphasize the differences between experimental conditions. The bar plot reports locomotor performance, which was quantified as the mean values \pm SEM of scores on PC1 (4). This analysis illustrates the graded improvement of locomotor performance under the progressive combination of chemical and bilateral electrical stimulation. Statistical test: Friedman test ANOVA. ***, P < 0.001. **(C)** To identify the specific features modulated with chemical and electrical stimulation, we extracted the parameters correlating with PC1 (factor loadings), and regrouped them into functional clusters, which we named for clarity. The numbers refer to variables described in **Table S1**. **(D)** Mean values \pm SEM of variables with high factor loadings, for each of the 5 functional clusters, as highlighted in panel C. Statistical test: Friedman test ANOVA. **, P < 0.01. *, P < 0.05. Error bars: standard error of mean, SEM.

PARAMETERS	VARIABLE	DETAILED EXPLANATION
KINEMATICS		
Temporal features		
	1	Cycle duration
	2	Cycle velocity
	3	Stance duration
	4	Swing duration
	5	Relative stance duration (percent of the cycle duration)
Limb endpoint (Metatarsal phalange) trajectory		
	6	Interlimb temporal coupling
	7	Duration of double stance phase
	8	Stride length
	9	Step length
	10	3D limb endpoint path length
	11	Maximum backward position
	12	Minimum forward position
	13	Step height
	14	Maximum speed during swing
	15	Relative timing of maximum velocity during swing
	16	Acceleration at swing onset
	17	Average endpoint velocity
	18	Orientation of the velocity vector at swing onset
	19	Dragging
	20	Relative dragging duration (percent of swing duration)
Stability		
<i>Base of support</i>	21	Positioning of the foot at stance onset with respect to the pelvis
	22	Stance width
Trunk and pelvic	23	Maximum hip sagittal position
	24	Minimum hip sagittal position
position and	25	Amplitude of sagittal hip oscillations
	26	Variability of sagittal crest position
oscillations	27	Variability of sagittal crest velocity
	28	Variability of vertical hip movement
	29	Variability of sagittal hip movement
	30	Variability of the 3D hip oscillations
	31	Length of pelvis displacements in the forward direction
	32	Length of pelvis displacements in the medio-lateral direction
	33	Length of pelvis displacements in the vertical direction
	34	Length of pelvis displacements in all directions
Joint angles and segmental oscillations		
<i>Backward</i>	35	Crest oscillations
	36	Thigh oscillations
	37	Leg oscillations
	38	Foot oscillations
	39	Whole limb oscillations
<i>Forward</i>	40	Crest oscillations
	41	Thigh oscillations
	42	Leg oscillations
	43	Foot oscillations
	44	Whole limb oscillations
<i>Flexion</i>	45	Hip joint angle
	46	Knee joint angle
	47	Ankle joint angle
<i>Abduction</i>	48	Whole limb abduction
	49	Foot abduction
<i>Extension</i>	50	Hip joint angle
	51	Knee joint angle
	52	Ankle joint angle

<i>Adduction</i>	53	Whole limb adduction
	54	Foot adduction
<i>Amplitude</i>	55	Crest oscillations
	56	Thigh oscillations
	57	Leg oscillations
	58	Foot oscillations
	59	Whole limb oscillations
	60	Hip joint angle
	61	Knee joint angle
	62	Ankle joint angle
	63	Whole limb medio-lateral oscillations
	64	Foot abduction/adduction
Velocity		
<i>Minimum</i>	65	Whole limb oscillation velocity
	66	Hip joint angle velocity
	67	Knee joint angle velocity
	68	Ankle joint angle velocity
<i>Maximum</i>	69	Whole limb oscillation velocity
	70	Hip joint angle velocity
	71	Knee joint angle velocity
<i>Amplitude</i>	72	Ankle joint angle velocity
	73	Whole limb angle velocity
	74	Hip joint angle velocity
	75	Knee joint angle velocity
	76	Ankle joint angle velocity
Inter-limb coordination		
<i>PC analysis</i>	77	Degree of linear coupling between joint oscillations
	78	Temporal coupling between crest and thigh oscillations
<i>FFT decomposition</i>	79	Temporal coupling between thigh and leg oscillations
	80	Temporal coupling between leg and foot oscillations
<i>Cross-correlation</i>	81	Correlation between crest and thigh oscillations
	82	Correlation between thigh and leg oscillations
	83	Correlation between leg and foot oscillations
	84	Correlation between hip and knee oscillations
	85	Correlation between knee and ankle oscillations
	86	Correlation between ankle and MTP oscillations
	87	Temporal lag between backward positions of crest and thigh oscillations
<i>Relative coupling</i>	88	Temporal lag between forward positions of crest and thigh oscillations
	89	Temporal lag between backward positions of thigh and leg oscillations
	90	Temporal lag between forward positions of the thigh and leg oscillations
	91	Temporal lag between backward positions of leg and foot oscillations
	92	Temporal lag between forward positions of leg and foot oscillations
<i>Inter-segmental coordination compared to</i>	93	Lag of the cross correlation function between hindlimb oscillations
	94	Maximum R-value of the cross correlation function between hindlimb oscillations
	95	Lag of the cross correlation function between hip oscillations
<i>Able-bodied rats</i>	96	Maximum R-value of the cross correlation function between hip oscillations
	97	Lag of the cross correlation function between knee oscillations
	98	Maximum R-value of the cross correlation function between knee oscillations
	99	Lag of the cross correlation function between ankle oscillations
	100	Maximum R-value of the cross correlation function between ankle oscillations
	101	Lag of the cross correlation function between endpoint oscillations
	102	Maximum R-value of the cross correlation function between endpoint oscillations
	103	Phase of the first harmonic of the FFT of the hip elevation angle
104	Amplitude of the first harmonic of the FFT of the hip elevation angle	

	105	Phase of the first harmonic of the FFT of the knee elevation angle
	106	Amplitude of the first harmonic of the FFT of the knee elevation angle
	107	Phase of the first harmonic of the FFT of the ankle elevation angle
Left-right	108	Amplitude of the first harmonic of the FFT of the ankle elevation angle
	109	Phase of the first harmonic of the FFT of the endpoint elevation angle
	110	Amplitude of the first harmonic of the FFT of the endpoint elevation angle
hindlimb	111	Phase of the first harmonic of the FFT of the hindlimb elevation angle
	112	Amplitude of the first harmonic of the FFT of the hindlimb elevation angle
coordination	113	Lag of the cross correlation function between crest and thigh limb elevation angles
Hindlimb	114	Lag of the cross correlation function between thigh and hindlimb elevation angles
coordination	115	Lag of the cross correlation function between hip and thigh elevation angles
	116	Lag of the cross correlation function between hindlimb and foot elevation angles
	117	Lag of the cross correlation function between thigh and ankle elevation angles
	118	Lag of the cross correlation function between ankle and foot elevation angles
KINETICS		
	119	Medio-lateral forces
	120	Anteroposterior forces
	121	Vertical forces
	122	Weight-bearing level
MUSCLE ACTIVITY		
Timing (relative to cycle duration, paw contact to paw contact)		
<i>Extensor</i>	123	Relative onset of ipsilateral extensor muscle activity burst
	124	Relative end of ipsilateral extensor muscle activity burst
<i>Flexor</i>	125	Relative onset of ipsilateral flexor muscle activity burst
	126	Relative end of ipsilateral flexor muscle activity burst
Duration		
<i>Extensor</i>	127	Duration of ipsilateral extensor muscle activity burst
<i>Flexor</i>	128	Duration of ipsilateral flexor muscle activity burst
Amplitude		
<i>Extensor</i>	129	Mean amplitude of ipsilateral muscle activity burst
	130	Integral of ipsilateral extensor muscle activity burst
	131	Root mean square of ipsilateral extensor muscle activity burst
<i>Flexor</i>	132	Mean amplitude of ipsilateral flexor muscle activity burst
	133	Integral of ipsilateral flexor muscle activity burst
	134	Root mean square of ipsilateral flexor muscle activity burst
<i>Muscle coactivation</i>	135	Co-contraction of flexor and extensor muscle

Table S1: Computed kinematic, ground reaction force, and muscle activity variables.

References and Notes

1. D. Borton, S. Micera, J. R. Millán, G. Courtine, Personalized neuroprosthetics. *Sci. Transl. Med.* **5**, 210rv2 [Medline](#) and [doi:10.1126/scitranslmed.3005968](https://doi.org/10.1126/scitranslmed.3005968) (2013).
2. D.-H. Kim, J. Viventi, J. J. Amsden, J. Xiao, L. Vigeland, Y. S. Kim, J. A. Blanco, B. Panilaitis, E. S. Frechette, D. Contreras, D. L. Kaplan, F. G. Omenetto, Y. Huang, K. C. Hwang, M. R. Zakin, B. Litt, J. A. Rogers, Dissolvable films of silk fibroin for ultrathin conformal bio-integrated electronics. *Nat. Mater.* **9**, 511–517 [Medline](#) and [doi:10.1038/nmat2745](https://doi.org/10.1038/nmat2745) (2010).
3. P. Fattahi, G. Yang, G. Kim, M. R. Abidian, A review of organic and inorganic biomaterials for neural interfaces. *Adv. Mater.* **26**, 1846–1885 [Medline](#) and [doi:10.1002/adma.201304496](https://doi.org/10.1002/adma.201304496) (2014).
4. R. van den Brand, J. Heutschi, Q. Barraud, J. DiGiovanna, K. Bartholdi, M. Huerlimann, L. Friedli, I. Vollenweider, E. M. Moraud, S. Duis, N. Dominici, S. Micera, P. Musienko, G. Courtine, Restoring voluntary control of locomotion after paralyzing spinal cord injury. *Science* **336**, 1182–1185 [Medline](#) and [doi:10.1126/science.1217416](https://doi.org/10.1126/science.1217416) (2012).
5. D. W. Park, A. A. Schendel, S. Mikael, S. K. Brodnick, T. J. Richner, J. P. Ness, M. R. Hayat, F. Atry, S. T. Frye, R. Pashaie, S. Thongpang, Z. Ma, J. C. Williams, Graphene-based carbon-layered electrode array technology for neural imaging and optogenetic applications. *Nat. Commun.* **5**, 5258 [Medline](#) and [doi:10.1038/ncomms6258](https://doi.org/10.1038/ncomms6258) (2014).
6. J. C. Barrese, N. Rao, K. Paroo, C. Triebwasser, C. Vargas-Irwin, L. Franquemont, J. P. Donoghue, Failure mode analysis of silicon-based intracortical microelectrode arrays in non-human primates. *J. Neural Eng.* **10**, 066014 [Medline](#) and [doi:10.1088/1741-2560/10/6/066014](https://doi.org/10.1088/1741-2560/10/6/066014) (2013).
7. P. Moshayedi, G. Ng, J. C. Kwok, G. S. Yeo, C. E. Bryant, J. W. Fawcett, K. Franze, J. Guck, The relationship between glial cell mechanosensitivity and foreign body reactions in the central nervous system. *Biomaterials* **35**, 3919–3925 [Medline](#) and [doi:10.1016/j.biomaterials.2014.01.038](https://doi.org/10.1016/j.biomaterials.2014.01.038) (2014).
8. K. A. Potter, M. Jorfi, K. T. Householder, E. J. Foster, C. Weder, J. R. Capadona, Curcumin-releasing mechanically adaptive intracortical implants improve the proximal neuronal density and blood-brain barrier stability. *Acta Biomater.* **10**, 2209–2222 [Medline](#) and [doi:10.1016/j.actbio.2014.01.018](https://doi.org/10.1016/j.actbio.2014.01.018) (2014).
9. Y.-B. Lu, K. Franze, G. Seifert, C. Steinhäuser, F. Kirchhoff, H. Wolburg, J. Guck, P. Janmey, E. Q. Wei, J. Käs, A. Reichenbach, Viscoelastic properties of individual glial cells and neurons in the CNS. *Proc. Natl. Acad. Sci. U.S.A.* **103**, 17759–17764 (2006). [Medline](#) [doi:10.1073/pnas.0606150103](https://doi.org/10.1073/pnas.0606150103)
10. B. S. Elkin, A. I. Ilankovan, B. Morrison 3rd, A detailed viscoelastic characterization of the P17 and adult rat brain. *J. Neurotrauma* **28**, 2235–2244 [Medline](#) and [doi:10.1089/neu.2010.1604](https://doi.org/10.1089/neu.2010.1604) (2011).
11. A. F. Christ, K. Franze, H. Gautier, P. Moshayedi, J. Fawcett, R. J. Franklin, R. T. Karadottir, J. Guck, Mechanical difference between white and gray matter in the rat

- cerebellum measured by scanning force microscopy. *J. Biomech.* **43**, 2986–2992 [Medline](#) and [doi:10.1016/j.jbiomech.2010.07.002](https://doi.org/10.1016/j.jbiomech.2010.07.002) (2010).
12. B. S. Elkin, E. U. Azeloglu, K. D. Costa, B. Morrison 3rd, Mechanical heterogeneity of the rat hippocampus measured by atomic force microscope indentation. *J. Neurotrauma* **24**, 812–822 [Medline](#) and [doi:10.1089/neu.2006.0169](https://doi.org/10.1089/neu.2006.0169) (2007).
 13. D. R. Enzmann, N. J. Pelc, Brain motion: Measurement with phase-contrast MR imaging. *Radiology* **185**, 653–660 [Medline](#) and [doi:10.1148/radiology.185.3.1438741](https://doi.org/10.1148/radiology.185.3.1438741) (1992).
 14. D. E. Harrison, R. Cailliet, D. D. Harrison, S. J. Troyanovich, S. O. Harrison, A review of biomechanics of the central nervous system—Part I: Spinal canal deformations resulting from changes in posture. *J. Manipulative Physiol. Ther.* **22**, 227–234 [doi:10.1016/S0161-4754\(99\)70049-7](https://doi.org/10.1016/S0161-4754(99)70049-7) (1999). [Medline](#)
 15. P. Konrad, T. Shanks, Implantable brain computer interface: Challenges to neurotechnology translation. *Neurobiol. Dis.* **38**, 369–375 [Medline](#) and [doi:10.1016/j.nbd.2009.12.007](https://doi.org/10.1016/j.nbd.2009.12.007) (2010).
 16. P. Musienko, R. van den Brand, O. Maerzendorfer, A. Larmagnac, G. Courtine, Combinatory electrical and pharmacological neuroprosthetic interfaces to regain motor function after spinal cord injury. *IEEE Trans. Biomed. Eng.* **56**, 2707–2711 [Medline](#) and [doi:10.1109/TBME.2009.2027226](https://doi.org/10.1109/TBME.2009.2027226) (2009).
 17. S. P. Lacour, D. Chan, S. Wagner, T. Li, Z. Suo, Mechanisms of reversible stretchability of thin metal films on elastomeric substrates. *Appl. Phys. Lett.* **88**, 204103 [doi:10.1063/1.2201874](https://doi.org/10.1063/1.2201874) (2006).
 18. A. Mailis-Gagnon, A. D. Furlan, J. A. Sandoval, R. Taylor, Spinal cord stimulation for chronic pain. *Cochrane Database Syst. Rev.* (3): CD003783 [Medline](#) (2004).
 19. C. A. Angeli, V. R. Edgerton, Y. P. Gerasimenko, S. J. Harkema, Altering spinal cord excitability enables voluntary movements after chronic complete paralysis in humans. *Brain* **137**, 1394–1409 [Medline](#) and [doi:10.1093/brain/awu038](https://doi.org/10.1093/brain/awu038) (2014).
 20. P. Gad, J. Choe, M. S. Nandra, H. Zhong, R. R. Roy, Y. C. Tai, V. R. Edgerton, Development of a multi-electrode array for spinal cord epidural stimulation to facilitate stepping and standing after a complete spinal cord injury in adult rats. *J. Neuroeng. Rehabil.* **10**, 2 [Medline](#) and [doi:10.1186/1743-0003-10-2](https://doi.org/10.1186/1743-0003-10-2) (2013).
 21. NeuroNexus, Surface Probes. <http://neuronexus.com/products/neural-probes/surface-probes>, (2014).
 22. C. F. Guo, T. Sun, Q. Liu, Z. Suo, Z. Ren, Highly stretchable and transparent nanomesh electrodes made by grain boundary lithography. *Nat. Commun.* **5**, 3121 [Medline](#) and [doi:10.1038/ncomms4121](https://doi.org/10.1038/ncomms4121) (2014).
 23. J. A. Fan, W. H. Yeo, Y. Su, Y. Hattori, W. Lee, S. Y. Jung, Y. Zhang, Z. Liu, H. Cheng, L. Falgout, M. Bajema, T. Coleman, D. Gregoire, R. J. Larsen, Y. Huang, J. A. Rogers, Fractal design concepts for stretchable electronics. *Nat. Commun.* **5**, 3266 [Medline](#) and [doi:10.1038/ncomms4266](https://doi.org/10.1038/ncomms4266) (2014).
 24. J. Vanfleteren, I. Chtioui, B. Plovie, Y. Yang, F. Bossuyt, T. Vervust, S. Dunphy, B. Vandecasteele, Arbitrarily Shaped 2.5D Circuits Using stretchable interconnections and

- embedding in thermoplastic polymers. *Procedia Technol.* **15**, 208–215 (2014).
[doi:10.1016/j.protcy.2014.09.073](https://doi.org/10.1016/j.protcy.2014.09.073)
25. D.-H. Kim, R. Ghaffari, N. Lu, S. Wang, S. P. Lee, H. Keum, R. D'Angelo, L. Klinker, Y. Su, C. Lu, Y. S. Kim, A. Ameen, Y. Li, Y. Zhang, B. de Graff, Y. Y. Hsu, Z. Liu, J. Ruskin, L. Xu, C. Lu, F. G. Omenetto, Y. Huang, M. Mansour, M. J. Slepian, J. A. Rogers, Electronic sensor and actuator webs for large-area complex geometry cardiac mapping and therapy. *Proc. Natl. Acad. Sci. U.S.A.* **109**, 19910–19915 [Medline](https://pubmed.ncbi.nlm.nih.gov/22511111/) and [doi:10.1073/pnas.1205923109](https://doi.org/10.1073/pnas.1205923109) (2012).
 26. S. F. Cogan, Neural stimulation and recording electrodes. *Annu. Rev. Biomed. Eng.* **10**, 275–309 [Medline](https://pubmed.ncbi.nlm.nih.gov/18711111/) and [doi:10.1146/annurev.bioeng.10.061807.160518](https://doi.org/10.1146/annurev.bioeng.10.061807.160518) (2008).
 27. U. A. Aregueta-Robles, A. J. Woolley, L. A. Poole-Warren, N. H. Lovell, R. A. Green, Organic electrode coatings for next-generation neural interfaces. *Front. Neuroeng.* **7**, 15 (2014). [Medline](https://pubmed.ncbi.nlm.nih.gov/25511111/) [doi:10.3389/fneng.2014.00015](https://doi.org/10.3389/fneng.2014.00015)
 28. T. Pistohl, A. Schulze-Bonhage, A. Aertsen, C. Mehring, T. Ball, Decoding natural grasp types from human ECoG. *Neuroimage* **59**, 248–260 [Medline](https://pubmed.ncbi.nlm.nih.gov/22511111/) and [doi:10.1016/j.neuroimage.2011.06.084](https://doi.org/10.1016/j.neuroimage.2011.06.084) (2012).
 29. P. Musienko, R. van den Brand, O. Märzendorfer, R. R. Roy, Y. Gerasimenko, V. R. Edgerton, G. Courtine, Controlling specific locomotor behaviors through multidimensional monoaminergic modulation of spinal circuitries. *J. Neurosci.* **31**, 9264–9278 [Medline](https://pubmed.ncbi.nlm.nih.gov/22511111/) and [doi:10.1523/JNEUROSCI.5796-10.2011](https://doi.org/10.1523/JNEUROSCI.5796-10.2011) (2011).
 30. G. Courtine, Y. Gerasimenko, R. van den Brand, A. Yew, P. Musienko, H. Zhong, B. Song, Y. Ao, R. M. Ichiyama, I. Lavrov, R. R. Roy, M. V. Sofroniew, V. R. Edgerton, Transformation of nonfunctional spinal circuits into functional states after the loss of brain input. *Nat. Neurosci.* **12**, 1333–1342 [Medline](https://pubmed.ncbi.nlm.nih.gov/22511111/) and [doi:10.1038/nn.2401](https://doi.org/10.1038/nn.2401) (2009).
 31. L. E. Bilston, L. E. Thibault, The mechanical properties of the human cervical spinal cord in vitro. *Ann. Biomed. Eng.* **24**, 67–74 [Medline](https://pubmed.ncbi.nlm.nih.gov/22511111/) and [doi:10.1007/BF02770996](https://doi.org/10.1007/BF02770996) (1996).
 32. S. Cheng, E. C. Clarke, L. E. Bilston, Rheological properties of the tissues of the central nervous system: A review. *Med. Eng. Phys.* **30**, 1318–1337 (2008). [Medline](https://pubmed.ncbi.nlm.nih.gov/22511111/) [doi:10.1016/j.medengphy.2008.06.003](https://doi.org/10.1016/j.medengphy.2008.06.003)
 33. T. Saxena, J. L. Gilbert, J. M. Hasenwinkel, A versatile mesoindentation system to evaluate the micromechanical properties of soft, hydrated substrates on a cellular scale. *J. Biomed. Mater. Res. A* **90A**, 1206–1217 [Medline](https://pubmed.ncbi.nlm.nih.gov/22511111/) and [doi:10.1002/jbm.a.32178](https://doi.org/10.1002/jbm.a.32178) (2009).